Capacity Fade and Its Mitigation in Li-ion Cells with Silicon-Graphite Electrodes

Javier Bareño[1], Ilya A. Shkrob[1*], James A. Gilbert[1], Matilda Klett[1,2], and Daniel P. Abraham[1]

[1] *Chemical Sciences and Engineering Division, Argonne National Laboratory, Argonne, Illinois, 60439, USA*

ABSTRACT:

Silicon-graphite (Si-Gr) electrodes typically contain lithiated carboxylates as polymer binders that are introduced through aqueous processing. Li-ion cells with such electrodes show significantly faster capacity fade than cells with graphite (Gr) electrodes. Here we examine the causes for capacity loss in Si-Gr cells containing $LiPF_6$ based electrolytes. The presence of SiO_xF_y in the Si-Gr electrode, fluorophosphate species in the electrolyte, and silica on the positive electrode indicates the crucial role of the hydrolytic cycle. In particular, HF acid that is generated through $LiPF_6$ hydrolysis corrodes Si particles. As it reacts, the released water re-enters the cycle. We trace the moisture initiating this detrimental cycle to the hydration water in the lithiated binders that cannot be fully removed by thermal treatment. The rate of HF corrosion can be reduced through the use of electrolyte additives. For fluoroethylene carbonate (FEC) additive the improved performance arises from changes to the solid electrolyte interphase (SEI) that serves as a barrier against HF attack. We propose that the greater extent of polymer crosslinking, that gives FEC-derived SEI elastomer properties, slows down HF percolation through this SEI membrane and inhibits the formation of deep cracks through which HF can access and degrade the Si surface.

* Corresponding authors:

Daniel P. Abraham (abraham@anl.gov); Phone: 630-252-4332

Ilya A. Shkrob (shkrob@anl.gov); Phone: 630-252-9516

[2]Current address: *KTH Royal Institute of Technology, Stockholm, Sweden*

INTRODUCTION

Silicon-containing lithium-ion batteries are drawing increasing attention because of their ability to store more charge than conventional cells with graphite (Gr)-based electrodes. [1-3] The excessive volume expansion makes the use of pure silicon electrodes challenging, so electrodes containing silicon-graphite (Si-Gr) mixtures are frequently used instead. The chief concern with the Si-Gr cells is the capacity fade, which is significantly faster than that of Gr cells implicating silicon as the culprit. The capacity fade is mainly the consequence of lithium ion loss to the solid electrolyte interphase (SEI) that forms on the Si-Gr electrodes. Previous research [4-16] has implicated the erosion of Si particles by hydrofluoric acid (HF) as a leading cause of the electrochemical performance deterioration. This acid is generated, *inter alia*, when the $LiPF_6$ (electrolyte) salt is hydrolyzed by moisture. [17-21] The crucial difference between the Si and graphite particles is that HF readily reacts with Si and SiO_2 (that covers these Si particles initially), whereas it does not react with the graphite. The HF formation can be traced to stepwise hydrolytic cleavage of $LiPF_6$ by residual water present in the cell. The effect of this water differs dramatically for Gr and Si-Gr cells: while the effect is mild for cells with Gr electrodes, [22] water can have a significant effect on the performance of Si electrodes. Yoshida et al. [23] systematically studied the effect of added water on the cycling performance of electrodes composed of Si particles and carboxymethyl cellulose sodium salt (NaCMC) binder (Scheme 1). Cells with electrodes dried at 120 ºC showed lower initial reversible capacity and coulombic efficiency; performance improved when the electrodes were dried at 180 ºC, which was the practical limit due to thermal degradation of this binder.

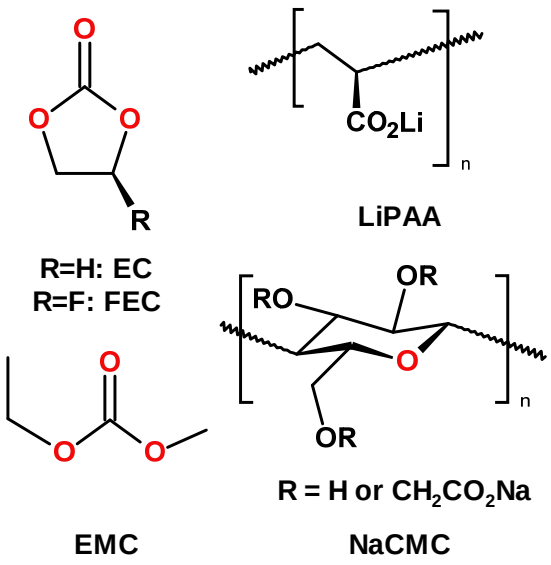

Scheme 1. Electrolyte Components: Ethylene Carbonate (EC), Fluoroethylene Carbonate (FEC), and Ethyl Methyl Carbonate (EMC). Two Common Polycarboxylate Binders: Lithiated Polyacrylic Acid (LiPAA) and Carboxymethyl Cellulose, Sodium Salt (NaCMC).

Another important difference between the Gr and Si-Gr electrodes is the chemical nature of polymer binders that are used to fabricate such electrodes. For Gr electrodes, the polymer binder is typically PVdF (polyvinylidene fluoride), a hydrophobic and inert polymer, and the organic solvent is *N*-methyl-2-pyrrolidone. For Si and Si-Gr electrodes, polycarboxylates (such as lithiated polyacrylic acid, LiPAA, and NaCMC, see Scheme 1) have been used instead, [24, 25] as (unlike PVdF) they form strong contacts with *all* of the particles present in the matrix. The Si-polymer binding is covalent in nature, as some of the siloxyl groups on the surface of Si/SiO_2 particles esterify carboxyl groups in the polymer chains. [26] As these polycarboxylate binders require aqueous processing (because these polymers do not readily dissolve in organic solvents), the materials are exposed to water during the fabrication process. Thus, a pertinent question is whether the moisture that is unavoidably introduced during Si-Gr electrode fabrication can be driven away

using common thermal treatments: we suggest that this might be impossible (or at least very difficult).

In this study we aim to establish the *role* of inadvertently introduced moisture in rapid capacity fade in Si-containing electrodes. Another goal is to explain how the adverse effects of HF acid generation by $LiPF_6$ hydrolysis can be mitigated using battery additives, including fluoroethylene carbonate (FEC, Scheme 1) that is used to improve SEI stability on Si-containing electrodes [27-29] Throughout this study our emphasis is mechanistic rather than practical. It is also holistic: while the *effects* of water are known, the *role* of this water, including its sources and sinks, and the chemical impact of the hydrolytic cycle in general remain insufficiently understood.

The supporting tables and figures have been placed in the Supporting Information (SI). When referenced in the text, these materials have the designator "S", as in Figure S1.

METHODS

Materials.

All electrodes examined in this study are from Argonne's Cell Analysis, Modeling, and Prototyping (CAMP) facility. The material compositions/sources and electrode characteristics are given in Table S1 in SI. The NCM523 (positive) electrode contains 90 wt% $Li_{1.03}(Ni_{0.5}Co_{0.2}Mn0_{.3})_{0.97}O_2$, 5 wt% carbons and 5 wt% PVdF binder. The Si-Gr (negative) electrode contains 73 wt% graphite, 15 wt% nanosilicon (50-70 nm), 2 wt% carbons, and 10 wt% LiPAA binder (450 kDa). [30] The latter is prepared by titration of PAA with LiOH to *pH* 6.3. The Gr (negative) electrode contain 88 wt% graphite, 2 wt% carbons, and 10 wt% LiPAA binder. After fabrication, all electrodes are stored in an Ar-atmosphere glove box (with <1 ppm H_2O). Prior to cell assembly for the electrochemical tests, the electrodes are vacuum-dried again. The NCM523

electrodes are dried for 3 h at 110 °C; the Si-Gr and Gr electrodes containing the water-based LiPAA binder are dried overnight in a vacuum oven at 150 °C. Our baseline (Gen2) electrolyte contains 1.2 M $LiPF_6$ in a 3:7 w/w mixture of ethylene carbonate (EC) and ethyl methyl carbonate (EMC) solvents (Scheme 1); cells with this electrolyte are referred to as the Gen2 cells. Some cells contained 10 wt% FEC added to the Gen2 electrolyte; these are referred to as the FEC-cells (this concentration of FEC was previously shown to be optimal). [31]

Electrochemical cell assembly and testing.

Most of our electrochemical tests were conducted in 2032-type coin cells (1.6 cm^2 area electrodes); some tests were conducted in larger cells with 20.3 cm^2 area electrodes. All cells were assembled in an Ar-atmosphere glove box. The electrolyte content of all cells was ~20 μL per cm^2 of the electrode. The cell testing protocol consisted of three (formation) cycles at a nominal C/20 rate, 94 (aging) cycles at a C/3 rate, and three (final) cycles at a C/20 rate, for a total of 100 cycles in the 2.5-4.1 V voltage range at 30 °C. This protocol was repeated multiple times for cells tested beyond 100 cycles. The *initial* negative-to-positive electrode capacity ratio, for cells cycled in the 2.5 V to 4.1 V range, was 1.3. The C-rates listed above are based on the initial C/1 capacity (~140 mAh/g_{oxide}) of the cells; these rates are not revised to account for the cell capacity loss during cycling. We emphasize that the entire inventory of cycled lithium in these full cells was introduced through the positive electrode, so the specific capacities given in this study are per weight of the *lithiated oxide* material in the *positive* electrode. In studies, where we probed specific capacity of the *negative* electrode, we summed the weights of silicon, graphite, and C45 carbon, which are all electrochemically active materials.

NMR Experiments.

These experiments were conducted on electrolytes obtained from the larger (20.3 cm^2 electrode) cells, which were much easier to disassemble in a glove box. Polyethylene pipettes and containers were used to extract and store the electrolytes, which were mixed with 1:20 v/v anhydrous CD_3CN; these solutions were subsequently analyzed using a Bruker Avance III HD 300 MHz spectrometer. ^{1}H, ^{13}C, ^{19}F, ^{31}P, and ^{29}Si nuclear magnetic resonance (NMR) spectra were obtained during the experiments.

XPS Experiments.

X-ray photoelectron spectroscopy (XPS) data were obtained using PHI 5000 VersaProbe II system from Physical Electronics using Al *Kα* radiation (1486.6 eV, 100 μm diameter at focus, 25 W), Ar^+ and electron beam sample neutralization, and fixed analyzer transmission mode. The samples were inserted into the XPS analysis chamber through an Ar atmosphere glovebox, without exposure to ambient air. Positive and negative electrodes harvested from the cycled cells were examined, after a light rinse with dimethyl carbonate to remove electrolyte residue. Peak fits of the XPS data were performed using the Shirley background correction and Gaussian-Lorentzian curve synthesis available in the CasaXPS suite. Element concentrations were calculated using integrated peak intensities and atomic relative sensitivity factors calibrated by the instrument manufacturer. For each sample the spectrum intensities (I) were normalized to reflect these calculated element concentrations.

Thermogravimetry.

To quantify water loss from LiPAA, an aqueous solution containing 10 wt% LiPAA was first evaporated to a thick slurry and then water was removed at 120 ºC over 5 h in a vacuum oven. The material was subsequently equilibrated with water vapor for 40 h under ambient conditions.

The thermogravimetry was carried out in helium flow using a Perkin Elmer Pyris 1TGA thermogravimetric analyzer coupled to a Perkin Elmer Clarus 680 gas chromatograph – mass spectrometer. The loaded sample was first held at 50 ºC for 1 min, then the temperature was ramped to 150 ºC at 6 ºC/min; the sample was held at 150 ºC for 14.5 h. Subsequently the temperature was increased to 400 ºC at 6 ºC/min. The linear mass loss due to pyrolysis began at 250 ºC (resulting in 10% weight loss at 400 ºC); hence, the mass at 225 ºC was taken as the dry weight.

RESULTS AND DISCUSSION

Electrochemistry data on full cells and component electrodes.

Electrochemical data from the NCM523/Si-Gr full cells are similar to those reported previously [30, 32] and are only briefly described here. Figure 1 shows discharge capacities as a function of cycle number for typical Gen2 and FEC cells. The inset table shows discharge capacities from cycle 1 (Initial, I) and cycle 100 (Final, F), respectively; these were obtained at a ~C/20 nominal rate. Figure 1 indicates that the Gen2 and FEC cell capacities are similar during the early (< 10) cycles. Subsequently, the Gen2 cell shows rapid capacity decrease, whereas the FEC cell shows a more gradual capacity decrease. After 100 cycles, the capacity loss for the Gen2 and FEC cell are 91.8% and 53.5%, respectively. In contrast, an NCM523/Gr full cell, containing Gen2 + 10 wt% FEC electrolyte, shows ~9% capacity loss after 100 cycles (Figure S1 in SI). The only difference between these cells is the presence of 15 wt% Si nanoparticles in the Si-Gr negative electrode.

To determine effect of aging on electrode capacities, we assembled half cells using positive and negative electrodes harvested from the 100 cycle NCM523/Si-Gr cells, using fresh separators and electrolyte; the electrodes were *not rinsed* prior to cell assembly. The harvested electrode data

were then compared with data from half cells prepared with pristine positive and negative electrodes cycled under the same conditions: see typical data in Figure S2 of SI. The data showed that positive electrodes harvested from both the 100-cycle Gen2 and FEC full cells have capacities comparable to that that of the pristine electrode. In contrast, negative electrodes harvested from Gen2 cells showed little capacity (20 mAh/g of Si, Graphite, C45) compared to the value of ~800 mAh/g for the pristine electrode. Remarkably, even the (75 wt%) graphite in the harvested electrode does not contribute to cell capacity, which indicates that almost all the active particles, whether silicon or graphite, become isolated by SEI deposits formed during cell cycling. On the other hand, negative electrodes harvested from FEC cells showed capacities that were mostly similar to that of the pristine electrode, indicating that capacity fade in these cells is dominated by Li inventory loss to the SEI covering silicon particles.

NMR characterization of electrolyte.

As corrosion of (either lithiated or delithiated) Si/SiO_2 particles by hydrolytically generated HF is thought to be the prime factor in the capacity fade, NMR spectroscopy was used to estimate the degree of $LiPF_6$ hydrolysis in the electrolyte. No ^{29}Si resonances were found in these electrolyte solutions. ^{19}F and ^{31}P NMR spectra (Figures S3 and S4 in SI) indicated advanced hydrolysis of $LiPF_6$. Three sets of doublets were observed in ^{19}F NMR spectra with their chemical shifts between -79 and -70 ppm vs. $CFCl_3$ (Table S2 and Figure S3 in SI) and the corresponding three multiplets: a septet, a triplet, and a doublet were observed in ^{31}P NMR spectra (Table S2 and Figure S4 in SI) that indicated coupling to six, two and one fluorine-19 nuclei. By matching *J*-coupling constants in these ^{31}P and ^{19}F multiplets (Table S2 in SI) the progenitors of the resonance lines were identified as, respectively, hexafluorophosphate (PF_6^-), difluorophosphate ($PO_2F_2^-$) and monofluorophosphate (PO_3F^{2-}) anions (or their esters). Their relative concentration in the

electrolyte was established by integration of the corresponding resonance lines (Table S2 in SI). According to this analysis, the presence of FEC did not have a significant effect on the extent of $LiPF_6$ hydrolysis.

XPS characterization of electrodes.

In this section we use X-ray photoelectron spectroscopy to demonstrate significant chemical changes in the negative electrode due to hydrolytic degradation of $LiPF_6$ in Si-graphite cells; we also demonstrate retardation of these changes in the presence of FEC additive. Furthermore, we establish that HF acid corrosion of Si particles has an indirect effect on the *positive* electrode, as silicon becomes transferred through the electrolyte and deposited on the surface of the *positive* electrode. For these XPS examinations, electrodes were harvested from cells held at 2.5 V for 24 h before disassembly; thus, the negative and positive electrodes are in the delithiated and lithiated states, respectively. Table 1 gives the cell configuration and cycling conditions and Figure S5 in SI summarizes the elemental compositions obtained from the XPS data. Because the ejected photoelectrons arise from the top 3 nm of the electrode, [33] as particles become covered with the SEI, these deposits become the main contributors to the overall XPS spectra.

***Negative Electrode*:** Many of the features observed for our Si-Gr electrodes are similar to the ones reported for Si and Gr electrodes, respectively. [7-11] The C *1s* spectrum (Figure 2a) of the pristine Si-Gr electrode (trace i) shows intensities arising from the graphite and LiPAA binder. [34] The graphite peak decreases significantly after formation cycling, and is not seen after 100 cycles for either the Gen2 (trace iv) or FEC (trace vi) cell, as the graphite becomes buried under SEI deposits. A similar observation can be made about the LiPAA binder peaks. Peak intensities centered around

286.5 eV (R-O), 288.5 eV (R=O), and in the 290-292 eV range (R-OCO_2 semicarbonates), where R=C_xH_y, are observed in the cycled electrodes; these signals arise from the SEI that includes various alkyl (semi)carbonates [35, 36] and fluorophosphates. [37] Overlapping with these R-O peaks are the C-H peaks from the polymeric component in the SEI. [7-11] The extensive formation of polymeric materials and semicarbonates in SEI has also been reported by Grey and co-workers using *in situ* solid-state NMR spectroscopy. [15, 38] For Gen2 cells (traces iii and iv), the decrease in 286.5 eV and 290-292 eV intensities for the 100 cycle electrode (relative to the 3-cycle electrode) suggests that these alkyl carbonates are being covered by compounds that include fluorophosphates, as cell aging proceeds. The FEC cells (traces v and vi), however, do not show a decrease in the alkyl carbonate intensities.

For the Si *2p* spectra (Figure 2d), we base our attributions on refs. [7-11]. The Si *2p* spectrum from the pristine electrode (trace i) shows two strong peaks, near 100 eV (Si) and 104 eV (SiO_2 shell). After 3 cycles, both the Gen2 (trace iii) and FEC (trace v) cells show intensities around 99.5 eV from amorphous silicon. [1] For the Gen2 cell, strong intensities are also seen in the 102–105 eV range, suggesting the presence of (in decreasing order) Li_xSiO_y (102.8 eV), SiO_2 (104 eV) and SiO_xF_y (105 eV) compounds. The FEC cell shows relatively weaker Li_xSiO_y intensities, and negligible SiO_2 and SiO_xF_y intensities, suggesting *inhibited HF acidolysis of Si/SiO_2 particle*s. After 100 cycles, the Gen2 cell (trace iv), shows negligible intensity in the 98.5-100.5 eV range indicating complete coverage of the silicon particles by SEI deposits that include SiO_xF_y species. In contrast, the FEC spectrum (trace vi) shows weak Si and Li_xSiO_y intensities and negligible SiO_xF_y signals.

Parallel developments are seen in the F *1s* spectra (Figure 2c). After 3 cycles, both Gen2 and FEC electrodes (traces iii and v) display intensities in the 686-688 eV range (LiF and P-F

bonds in $Li_xPF_yO_z$) and in the 688-690 eV range (O=P-F bonds in $Li_xPF_yO_z$). Using ^{19}F NMR of aged Si electrodes, Grey and co-workers [15] also observed $LiP_xO_yF_z$ species along with trapped $LiPF_6$ and LiF (see also ref. [4]). After 100 cycles, the Gen2 sample (trace iv) shows a large increase in both 686-688 eV and 688-690 eV ranges indicating substantial hydrolysis of $LiPF_6$. The FEC electrode (trace vi) shows an increase in the 688-690 eV signals but a small decrease in the 687-688 eV signals, indicating slower generation of the F-rich species.

Signals consistent with increasing $LiPF_6$ salt hydrolysis on aging are also seen in the P *2p* spectra (Figure 3b). For the Gen 2 samples (traces iii and iv), both P-F signals (137-139 eV) and P-O signals (around 134-136 eV) increase on aging. Changes are seen for the FEC samples, too (traces v and vi). For the 3-cycle Gen2 samples, there is a large disparity in Li *1s* vs. F *1s* signals (18.4 at% vs. 5.4 at% for Gr cell and 22.6 at% vs. 8% for Si-Gr cell). This suggests that most Li trapped at this initial stage is in the form of solvent (EC, EMC) breakdown products (such as alkyl carbonates), and Li_xSiO_y compounds. As the cells are aged, the lithium-to-fluorine ratio becomes closer to parity: 20.1 at% vs. 29.3 at% for the Si-Gr Gen2 cell (Figure S5 in SI). The higher F content is consistent with increasing LiF and SiO_xF_y content in the SEI. For the FEC cells, the Li *1s* vs. F *1s* ratio is 17.5 at% to 11.9 at% (3-cycle), and 16.3 at% to 12.3 at% (100-cycle); the smaller changes are again consistent with a more stable negative electrode SEI in the FEC cell.

The O *1s* spectra (Figure 2b) and Li *1s* spectra (Figure 3a) also show changes on aging; these plots are harder to interpret as multiple species contribute to the spectral features. For both Gen2 and FEC samples, changes in the O *1s* spectra reflect the decrease in alkyl carbonate content (533.5 eV) as these compounds are increasingly buried under SEI products (535.5 eV).

***Positive Electrode*:** In Figures 3c, 3d and 4, we show XPS spectra obtained from the harvested *positive* electrode. The trends in the data are similar to those reported in ref. [39] The C *1s* spectra (Figure 4a) from the pristine electrode (trace i) shows show intensities arising from the C45 carbon black (285 eV) and PVdF binder (286.3 and 291 eV). On cycling, for both Gen2 and FEC cells the intensities arising from graphite and PVdF decrease, indicating coverage by mostly inorganic surface species. The graphite and PVdF intensities are observed even after 100 cycles (Figure 4a, traces iv and vi) indicating a relatively thin or non-uniform surface coverage.

The reduction in PVdF intensities on aging are also observed in the F *1s* spectra (Figure 4c). The pristine electrode contains a peak at 688.5 eV arising from C-F bonds in PVdF. After 3 cycles (traces iii and v), additional intensities around 685 eV signify the presence of LiF. After 100 cycles (traces iv and vi), strong intensities in the 686-687 eV range indicate the presence of $Li_xPF_yO_z$ compounds, which are the products of $LiPF_6$ decomposition and hydrolysis. Corresponding intensity increases on aging are also seen in the Li *1s* spectra (Figure 3c) and P *2p* spectra (Figure 3d).

The significant and unexpected new observation is the presence of silicon (~3 at%) on the positive electrode of the aged Gen2 cell (Figure 4d, trace iv). This signal stems from silicon dioxide (or lithium silicate). None of the other positive electrodes examined showed noteworthy Si *2p* intensities, indicating that (i) the deposition is enhanced by cycling, and (ii) the FEC additive hinders Si loss from the Si-Gr electrode and its deposition on the positive electrode. We conclude that advanced corrosion of Si particles by HF (that is indicated by XPS spectra of negative electrodes) yields a soluble product that diffuses through the electrolyte and becomes deposited on the positive electrode during cell cycling.

The source of moisture.

For the hydrolytic activity suggested by our NMR and XPS experiments, extraneous water needs to be introduced into the cell during assembly. Given that Si-containing negative electrodes are commonly processed from aqueous suspensions (as the SiO_2-adhesive polymers tend to be insoluble in organic solvents), the most obvious source of this moisture is the electrode matrix itself. In particular, lithiated polycarboxylates that are used as a binder can form stable hydrates (see below). Can this hydration water be removed by thermal treatment of the electrode? The experiments described below suggest otherwise.

To demonstrate that, thermogravimetry was carried out (see Figure 5). The hydrated LiPAA gel initially contained ~2.2 water molecules per monomer unit, and one-half of this water was quickly lost as the temperature increased to 150 ºC. For the next 3 h, the loss followed $t^{-0.5}$ behavior that is typical for diffusion-limited mass loss and then it settled into the exponential mode with 1/*e* time constant of 11 h. As seen from the plot, after 3-4 h at 150 ºC, ~ 0.1 mol.eq of water was retained in the sample, and 0.02 mol.eq was retained after 10-15 h.

We remind that alkali polyacrylates are well known to form thermally stable hydrates. At equilibrium with moist air, dry LiPAA adsorbs ~4 mol.eq. water. [40, 41] The loss of this hydration water from alkali polyacrylates is incomplete even after prolonged heating at 100 ºC in a nitrogen flow. [40-43] For lithium [40, 41] sodium, [42] and potassium [43] polyacrylates, ~0.5 mol.eq of water per monomer is retained even after several days of drying the material at 100 ºC under atmospheric pressure. This observation is in contrast to polyacrylic acid (PAA) that readily loses H-bound hydration water on heating to 100 ºC, with the residual moisture < 10^{-2} mol.eq. [40-43] These observations, and our present thermogravimetric analyses, suggest that water may not be

completely removed under conditions that are typically used in the fabrication of Si-Gr electrodes from LiPAA slurries.

While residual moisture in the binder matrix is undesirable, removing it by excessive heating could be even a greater problem. For alkali PAAs, loss of volatiles (~10%) is observed between 100 and 400 ºC. [44] General thermodynamic arguments suggest that Li^+/H^+ substitution in PAA can never be complete. [25] Thermogravimetry analyses [44-46] indicate that the onset for skeletal degradation of PAA is 260 ºC. Partial loss of water via anhydride formation was observed at ~200 ºC, [46] and decarboxylation was observed at ~150 ºC. [45] Whereas most of the hydration water in PAA is lost below 100 ºC, some of this water is retained, and dehydration becomes slow between 100 and 200 ºC, as also seen in Figure 5. Prolonged heating can become the *source* of trapped moisture, as water becomes eliminated from the polycarboxylate chains (Scheme 1) via the anhydride formation. The latter reaction was observed *in situ* by Lucht and co-workers [14] for electrodes dried at 150 ºC for 4 h. This consideration suggests that trapped moisture may *never* be fully removed by thermal treatment, from the electrodes processed from aqueous slurries using polycarboxylate binders: at lower temperatures the hydration water cannot be removed, whereas at higher temperatures the polymer matrix begins to decompose, eliminating water.

The hydrolytic cycle.

The retention of moisture in the electrode matrix has significant ramifications for chemical stability of Si particles: a schematic representation of these effects is shown in Figure 6. During cycling of pure Si electrodes [8, 15, 38] the gradual disappearance of Si and a concomitant increase of SiO_xF_y, Li_xSiO_y, LiF and $LiPO_xF_y$ are observed (Figure 6a). The advanced oxygen-by-fluorine substitution, and the gradual conversion of nonfluoride lithium salts to LiF, [47] can be readily

rationalized through reactions of HF acid generated via $LiPF_6$ hydrolysis, as shown in Figure 6b. [8, 20, 21, 37]. This hydrolysis is also directly implicated by our ^{19}F and ^{31}P NMR analyses of liquid electrolyte in the aged cells (see Figures S3 and S4 in SI).

The released HF acid can react with many potential targets, including LiOH, silica, silicon, lithium salts (such as alkoxides and alkyl carbonates) in the negative electrode, and (lithiated) transition metal oxides and hydroxides on the positive electrode, forming fluorides. Importantly, water is the side product of most of these reactions (Figure 6a). For example, surface silanol groups on silica readily react with HF yielding a fluoride and releasing a water molecule

$$\equiv Si\text{-}OH + HF \rightarrow \equiv Si\text{-}F + H_2O \qquad (1)$$

During the first cycle, the water in the electrode matrix transforms to LiOH. The analogous $–CO_2H$ to $–CO_2Li$ transformation has been observed by Nguyen et al., [14] and the presence of LiOH in the matrix was demonstrated by ^{7}Li NMR. [15] In the latter study, no LiOH was observed without a water-processed binder, suggesting that LiOH originated from residual moisture - just as we suggest. [15, 38] Subsequent hydrolysis of $LiPF_6$ releases HF (Figure 6b) that reacts with the various electrode components (Figure 6a) forming fluorides and reintroducing water (e.g., via reaction 1) which enters the hydrolytic cycle shown in Figure 6b. In this way, the residual moisture becomes chemically transformed from one hydrolytically active species to another, never becoming "lost" and always retaining its ability to generate HF acid via the reactions shown in Figure 6b.

At the advanced stage of O-by-F substitution, tetrafluorosilane (SiF_4) and/or hexafluorosilicic acid (H_2SiF_6) can be generated. [48] These are highly soluble compounds that diffuse out of the negative electrode (Figure 6a) and into the electrolyte before they hydrolyze there to the silicic acid (H_4SiO_4). The SiF_4 or H_2SiF_6 could reach the positive electrode and react

with the lithiated metal oxides (either directly or via hydrolysis) forming the corresponding fluorides and converting to SiO_2 (such reactions of transition metal oxides are even used for ore refinement). [49] In this manner, silicon is transferred from the negative to the positive electrode and becomes deposited at the layered oxide surface (see Figure 4d).

The release of HF is less consequential on the Gr electrode, as this material (unlike Si/SiO_2 particles) does not *directly* react with HF, so the latter is only converting various lithium salts in SEI to LiF. [50] This conversion does not change the thickness of mineral deposits in the inner SEI; nor does it change the concentration of trapped lithium in the SEI. The situation with Si-graphite or Si electrodes is different, as a significant fraction of HF can react *directly* with the Si containing components of the matrix. In this regard, the access of HF to the Si particle surface is as important as the generation of HF (Figures 6a and 6c). The volumetric changes in Si/Li_xSi particles introduce stress and cracks in the SEI layers covering Si particles (Figure 6c). As the SEI layer cracks, fresh electrolyte containing HF reacts with the reducing surfaces, and more SEI is formed (trapping more mobile Li^+ ions). In contrast, the Gr electrodes exhibit much smaller volumetric changes; the cracks develop slowly, and SEI growth is mainly diffusion-controlled. [51-54]

Thus, the extent of HF acidolysis and the resulting transformation and loss of Si depends not only on the generation of HF but also on the ability of SEI to maintain integrity during cycling and serve as a barrier to HF access. Below we argue that FEC-derived SEI serves as this barrier.

How FEC impedes HF corrosion.

Our NMR data suggest that the extent of $LiPF_6$ hydrolysis (and, consequently, HF release) is not altered significantly in the presence of FEC, yet FEC markedly improved the cycling performance. As demonstrated in our earlier articles, see, for example, refs. [30, 32] (where this is

demonstrated using *dQ/dV* scans) during the first cycle, FEC is reduced preferentially to EC. Our XPS experiments indicate that FEC-derived SEI impedes Si deposition on the positive electrode, despite the ongoing HF release, whereas the EC-derived SEI in Gen2 does not prevent this deposition. The implication of this result is that HF does not easily reach the Si particle surface when such FEC-derived SEI is formed.

To serve as a robust protective barrier, despite the continuous volumetric changes (Figure 6c), the FEC-derived SEI should have the properties of an elastomer membrane. Not only can an elastomer undergo plastic flow (as many polymers do), it also exhibits strain reversibility; this latter property requires that random coils in the matrix become crosslinked. Ideally, an elastomer has sufficient number of such crosslinks to provide strain reversibility, yet not enough crosslinks to interfere with the uncoiling of the polymer chains.

Reduction of carbonate electrolyte yields linear oligomers and polymers that do not crosslink. For the polymer component of SEI to have elastomer properties, there should be a mechanism for crosslinking of polymer chains that are derived specifically through reduction of FEC. Just such a mechanism was suggested in ref. [55] where we scrutinized the reduction pathways for FEC. The essence of our argument is schematically depicted in Figure 7: the precise nature of the polymer and polymerization pathways are less important than the general principle illustrated in these schemes. One or two electron reduction of EC yields carbonates that initiate radical and anionic polymerization of EC (concomitant with its ring-opening and partial elimination of CO_2); [56, 57] the resulting polymer (Figure 7a) contains $–CH_2CH_2O-$ and $-CH_2CH_2OC(O)O-$ units. Subsequent reduction of this polymer breaks the C-O bonds (so the carbonate groups become lithiated) and releases terminal *C*-centered radicals. Although these terminal radicals can recombine, the overall process does not result in crosslinking of the polymer chains; the resulting

outer SEI does not have elastomer properties. The analogous polymers derived from FEC internalize –CH_2CHF- groups; these groups are reduced in preference to the carbonate groups and yield LiF and also internal *C*-centered radicals shown in Figure 7b. When these internal radicals in different polymer chains recombine, these chains become covalently linked, and the extent of this crosslinking gradually increases as the polymer becomes reduced. In this manner, the FEC-derived outer SEI becomes increasingly elastomer-like.

On graphite (where the volume expansion is < 10%), this crosslinking and elastomer properties improve the SEI performance incrementally, as the less permeable SEI is thinner and its cracking during cell aging is less likely. On silicon this property can become critical, as the volume change is much greater. Yet even this "rubbery" SEI membrane has its limits: eventually, after many cycles, it becomes thicker and more mineralized; cracks develop and grow, and HF finally gets access to the particle surface causing capacity fade.

CONCLUSION

In this study, we examined NCM523/Si-Gr cells with the baseline electrolyte, consisting of 1.2 M $LiPF_6$ in a mixture of cyclic and acyclic carbonates, with and without 10 wt% FEC, a known retardant of capacity fade in Si-containing electrodes. These cells were subjected to 100+ cycles and the harvested electrodes were characterized by electrochemical and spectroscopic means. Extensive SEI formation in the negative electrode (with or without FEC) and Si deposition on the positive electrode (without FEC) were observed. The chemical patterns of these changes were consistent with advanced HF acidolysis of Si/SiO_2 particles. Solution NMR characterization of the electrolytes also indicated $LiPF_6$ hydrolysis that occurs regardless of FEC presence in solution. Once water becomes inadvertently introduced into the Si-containing electrode, it

continuously cycles through the system, yielding HF acid. This HF acid causes considerable damage to Si particles, while hydrolysis of $LiPF_6$ keeps on supplying fluoride anions for this cycle.

Our data suggest that FEC has a particular way to interfere with this hydrolytic cycle. Namely, the FEC-derived SEI serves as a superior barrier for HF access to Si/SiO_2 surface compared to the EC-derived SEI. We propose that a greater degree of polymer crosslinking renders elastomer properties to the FEC-derived outer SEI. [55] Such crosslinking gives FEC-derived polymers in SEI two desired features: (i) it makes the polymer matrix less penetrable by HF and water and (ii) the thin elastomer membrane maintains integrity during the expansion and contraction of Si/Li_xS particles. In fact, these two properties are closely related: SEI that does not have elastomer properties cracks during the volumetric changes, allowing HF to reach the surface of Si particles and react. Percolation of HF through the matrix also leads to corrosion of these Si particles, albeit at a slower pace. This corrosion causes accumulation of insoluble reaction products; eventually their buildup causes cracking of the outer SEI. In the process, HF is consumed and water is recovered. This water causes further $LiPF_6$ hydrolysis, so still more HF is generated, entering the hydrolytic cycle, and in this way the corrosion of Si particles becomes a runaway self-sustaining process. While FEC can retard this corrosion by maintaining a protective layer around Si particle, it can only stall this corrosion. As the SEI grows thicker and more rigid over time, cracks develop through which the HF accesses the surface, and the capacity becomes lost.

Given that HF plays such pivotal and dramatic roles in this capacity fade, it is noteworthy that a part of the problem is the presence of water in electrodes that are processed from aqueous solutions of polycarboxylate binders. This is especially vexing because it might be impossible to remove all of this matrix-trapped water, as high temperatures are needed to shift the hydration equilibria and release the water from the hydrates, whereas at such temperatures the residual –

CO_2H groups in the polycarboxylate binder decompose, releasing more water. If water cannot be removed from the matrix, then using lithium salts that do not hydrolyze and yield HF can be a way to address this problem; however, most of such salts are known to corrode aluminum current collectors; [58-61] finding alternatives to $LiPF_6$, thus, remains a continuing challenge for lithium-ion cells.

ASSOCIATED CONTENT

Supporting Information: A PDF file containing additional figures and tables. This material is available free of charge via the Internet at http://pubs.acs.org.

Acknowledgments

We are grateful to our many colleagues at Argonne, especially to S. Trask, B. Polzin, A. Jansen, K. Pupek, N. Dietz, C. Peebles, I. Bloom, B. Key and D. Dees. Support from the U.S. Department of Energy's Vehicle Technologies Program (DOE-VTP), specifically from Peter Faguy and Dave Howell, is gratefully acknowledged. The electrodes and electrolytes used in this article are from Argonne's Cell Analysis, Modeling and Prototyping (CAMP) Facility; the XPS and thermogravimetry data were acquired at Argonne's Post-Test Facility. Both facilities are supported within the core funding of the Applied Battery Research (ABR) for Transportation Program. The SEM images were acquired at the Argonne Center for Nanoscale Materials, which is supported by the U. S. Department of Energy, Office of Science, Office of Basic Energy Sciences, under Contract No. DE-AC02-06CH11357.

The submitted manuscript has been created by UChicago Argonne, LLC, Operator of Argonne National Laboratory ("Argonne"). Argonne, a U.S. Department of Energy Office of Science laboratory, is operated under Contract No. DE-AC02-06CH11357. The U.S. Government

retains for itself, and others acting on its behalf, a paid-up nonexclusive, irrevocable worldwide license in said article to reproduce, prepare derivative works, distribute copies to the public, and perform publicly and display publicly, by or on behalf of the Government.

Table 1.

XPS sample nomenclature. Samples are from full cells containing NCM523 positive and either Si-Gr or Gr negative electrodes. Electrolytes and cycle numbers are as shown.

Sample	Anode	# Cycles	Electrolyte
i	Si-Gr	0	No exposure
ii	Gr	3 [a]	Gen2
iii	Si-Gr	3 [a]	
iv		100	
v		3 [a]	Gen2 + 10wt% FEC
vi		100	

a) Formation cycles.

Figure Captions.

Figure 1.

Cell discharge capacity as a function of cycle number for NCM523/Si-Gr cells containing Gen2 (*open circles*) and Gen2 with 10 wt% FEC electrolytes (*open triangles*). The inset table shows the capacity fade (CF) values after 100 cycles: I and F refer to Initial (cycle 1) and Final (cycle 100) discharge capacities, respectively. On extended cycling, the FEC cell capacity continues to decrease; after 400 cycles the capacity loss is 91%, which is comparable to that of the Gen2 cell after 100 cycles.

Figure 2.

XPS spectra of harvested negative electrodes from cells in Table 1 (see inset in panel a for the color table): (i) pristine Si-Gr cell, (ii) Gr cell, after three formation cycles in Gen2, (iii) Si-Gr cell, after three formation cycles in Gen2, (iv) Si-Gr cell, aged in Gen2, (v) Si-Gr cell, three formation cycles in Gen2 containing FEC, (vi) Si-Gr cell, aged in Gen2 containing FEC.

Figure 3.

XPS spectra in (a,c) Li *1s* and (b,d) P *2p* bands from harvested (a,b) negative electrodes and (c,d) positive electrodes from disassembled cells (ii) to (vi) in Table 1 (see inset in panel a for the color table): (ii) Gr cell, after three formation cycles in Gen2, (iii) Si-Gr cell, after three formation cycles in Gen2, (iv) Si-Gr cell, aged in Gen2, (v) Si-Gr cell, three formation cycles in Gen2 containing FEC, (vi) Si-Gr cell, aged in Gen2 containing FEC.

Figure 4.

XPS spectra of harvested positive electrodes from cells (i) to (vi) in Table 1 (see inset in panel a for the color table): (i) pristine Si-Gr cell, (ii) Gr cell, after three formation cycles in Gen2, (iii) Si-Gr cell, after three formation cycles in Gen2, (iv) Si-Gr cell, aged in Gen2, (v) Si-Gr cell, three formation cycles in Gen2 containing FEC, (vi) Si-Gr cell, aged in Gen2 containing FEC. The spectral regions are indicated in the panels.

Figure 5.

Water loss from hydrated LiPAA binder as observed by thermogravimetry. Note the logarithmic vertical scale. The first section of the plot (indicated with the arrow) corresponds to heating of the sample from 50 to 150 ^{o}C at 6 ^{o}C/min, whereas the scattered dots indicate the 150 ^{o}C isotherm. After the first 3 hours, the mass loss settles into the exponential regime (*dashed line*).

Figure 6.

(a) Schematic representation of a Si particle in the advanced stages of aging, with the inner and outer SEI layers formed around the Si core. Mineral compounds derived from Si prevail in the inner SEI while various organic compounds (including alkyl carbonates and inner-carbonate polymers) prevail in the outer SEI, with insoluble salts trapped in the semisolid matrix. Electrolyte and HF molecules can diffuse through the pores and cracks in the outer SEI and react with the particle interior, releasing SiF_4 and water molecules back into the electrolyte. This water joins the hydrolytic cycle for $LiPF_6$ (shown in panel b). In the latter, water sequentially hydrolyzes PO_xF_y species, consuming five water molecules and releasing five HF molecules in total; the released HF can react with Si particles, continuing the hydrolytic cycle. The two species at the end of this sequence can be observed using NMR spectroscopy in the fluids collected from the aged cells. (c) As the Si particles repeatedly expand and contract during lithiation/delithiation, deep cracks develop allowing access of HF to the core, resulting in its digestion and additional SEI formation.

Figure 7.

Schematic rationalization of the observed morphological differences between the polymeric component of outer SEI derived from (a) ethylene carbonate (EC) and (b) fluoroethylene carbonate (FEC). In both cases we consider a matrix composed of polycarbonate oligomers generated via anionic polymerization of the corresponding carbonates. Further reduction of the polymer in panel (a) breaks C-O bonds yielding alkylcarbonates and *C*-centered terminal radicals on the neighboring polymer chains. Even if these radicals subsequently recombine, there is no crosslinking, so the cohesion of SEI matrix is not improved. The difference in panel b is that the reduction defluorinates the polymer chains yielding interior radicals whose subsequent recombination links these polymer chains, gradually converting these polymers into an elastomer matrix.

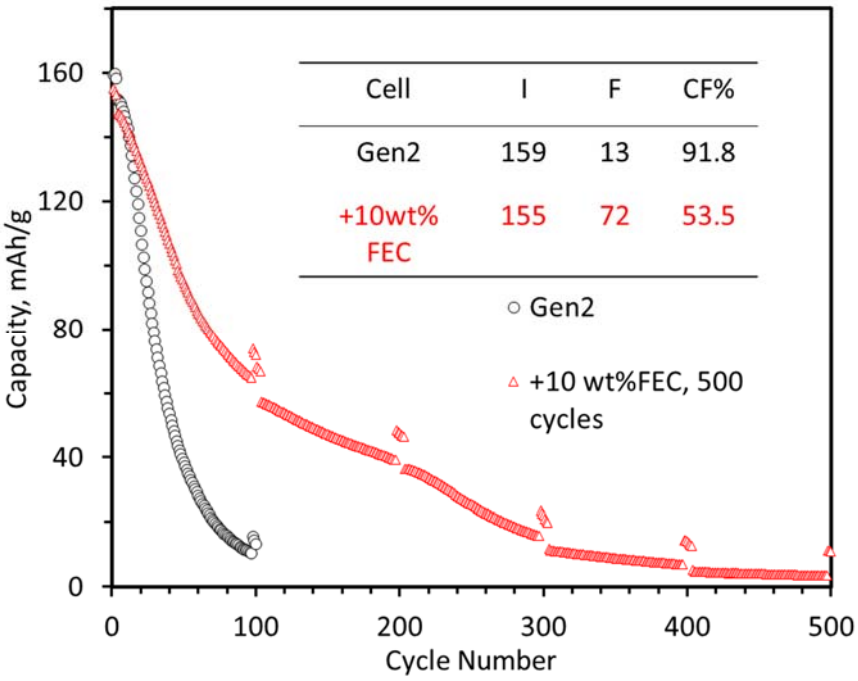

Figure 1. Cell discharge capacity (per weight of NCM523) as a function of cycle number for NCM523/Si-Gr cells containing Gen2 (*open circles*) and Gen2 with 10 wt% FEC electrolytes (*open triangles*). The inset table shows the capacity fade (CF) values after 100 cycles: I and F refer to Initial (cycle 1) and Final (cycle 100) discharge capacities, respectively. On extended cycling, the FEC cell capacity continues to decrease; after 400 cycles the capacity loss is 91%, which is comparable to that of the Gen2 cell after 100 cycles.

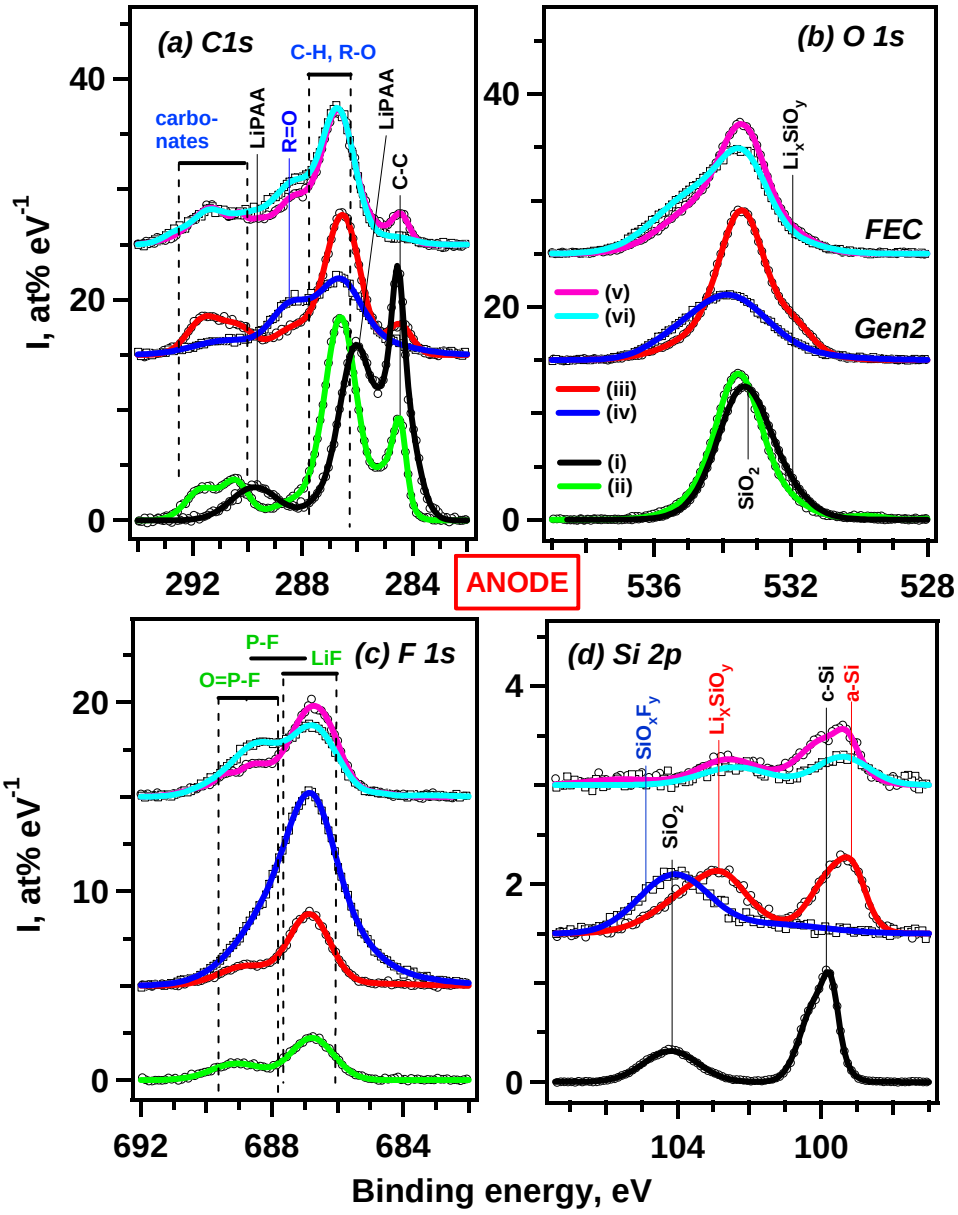

Figure 2. XPS spectra of harvested negative electrodes from cells in Table 1 (see inset in panel a for the color table): (i) pristine Si-Gr cell, (ii) Gr cell, after three formation cycles in Gen2, (iii) Si-Gr cell, after three formation cycles in Gen2, (iv) Si-Gr cell, aged in Gen2, (v) Si-Gr cell, three formation cycles in Gen2 containing FEC, (vi) Si-Gr cell, aged in Gen2 containing FEC.

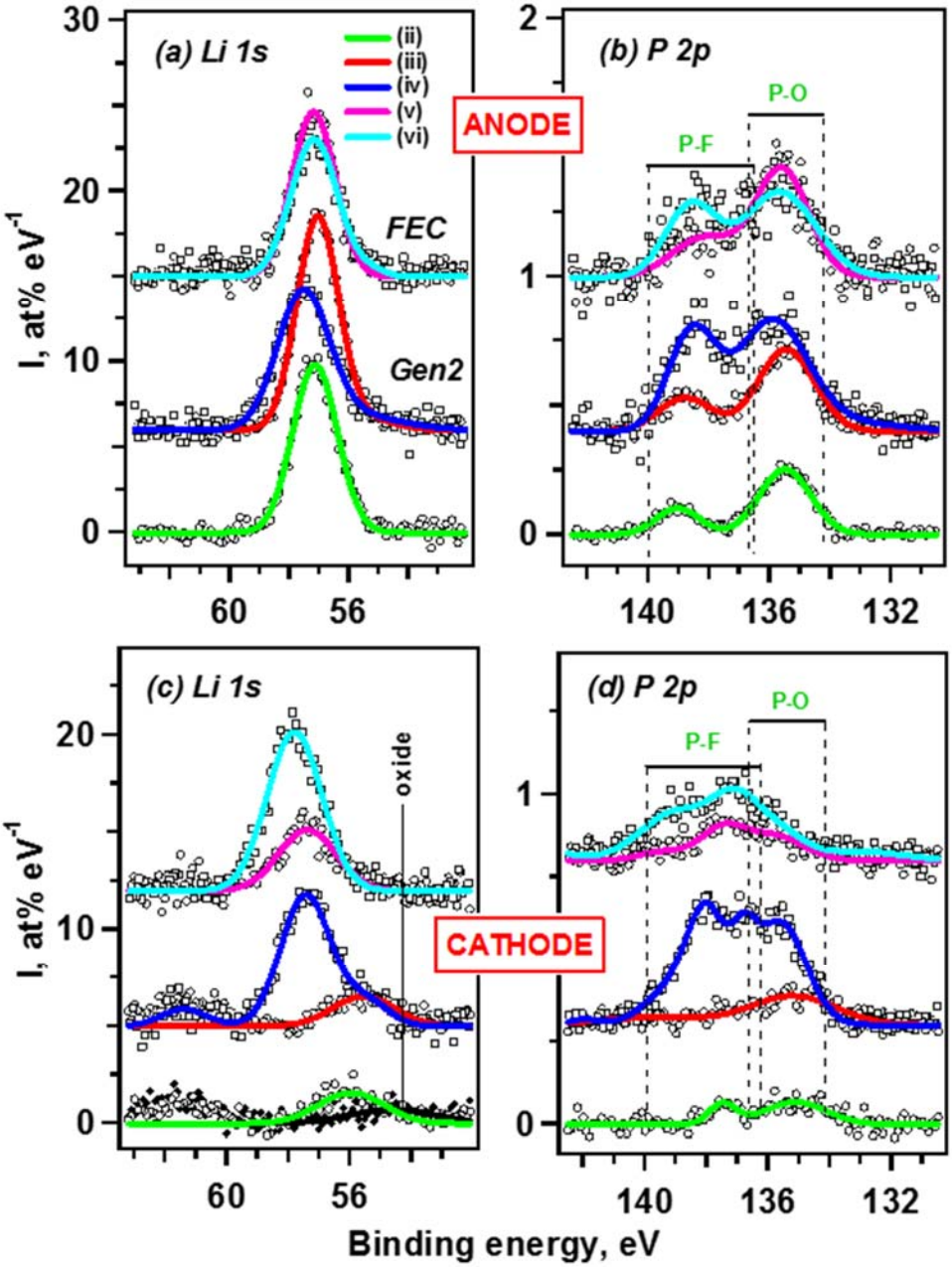

Figure 3. XPS spectra in (a,c) Li *1s* and (b,d) P *2p* bands from harvested (a,b) negative electrodes and (c,d) positive electrodes from disassembled cells (ii) to (vi) in Table 1 (see inset in panel a for the color table): (ii) Gr cell, after three formation cycles in Gen2, (iii) Si-Gr cell, after three formation cycles in Gen2, (iv) Si-Gr cell, aged in Gen2, (v) Si-Gr cell, three formation cycles in Gen2 containing FEC, (vi) Si-Gr cell, aged in Gen2 containing FEC.

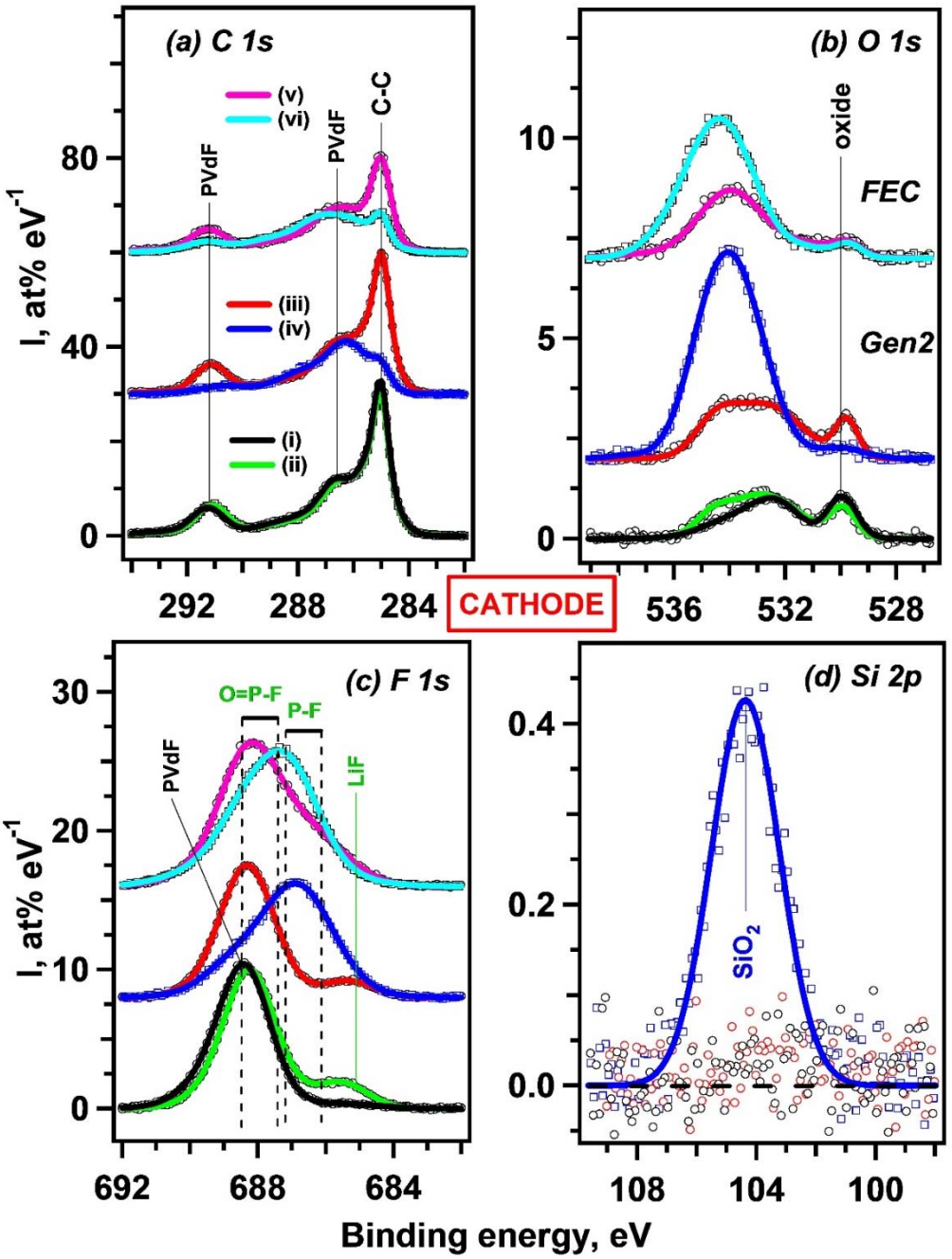

Figure 4. XPS spectra of harvested positive electrodes from cells (i) to (vi) in Table 1 (see inset in panel a for the color table): (i) pristine Si-Gr cell, (ii) Gr cell, after three formation cycles in Gen2, (iii) Si-Gr cell, after three formation cycles in Gen2, (iv) Si-Gr cell, aged in Gen2, (v) Si-Gr cell, three formation cycles in Gen2 containing FEC, (vi) Si-Gr cell, aged in Gen2 containing FEC. The spectral regions are indicated in the panels.

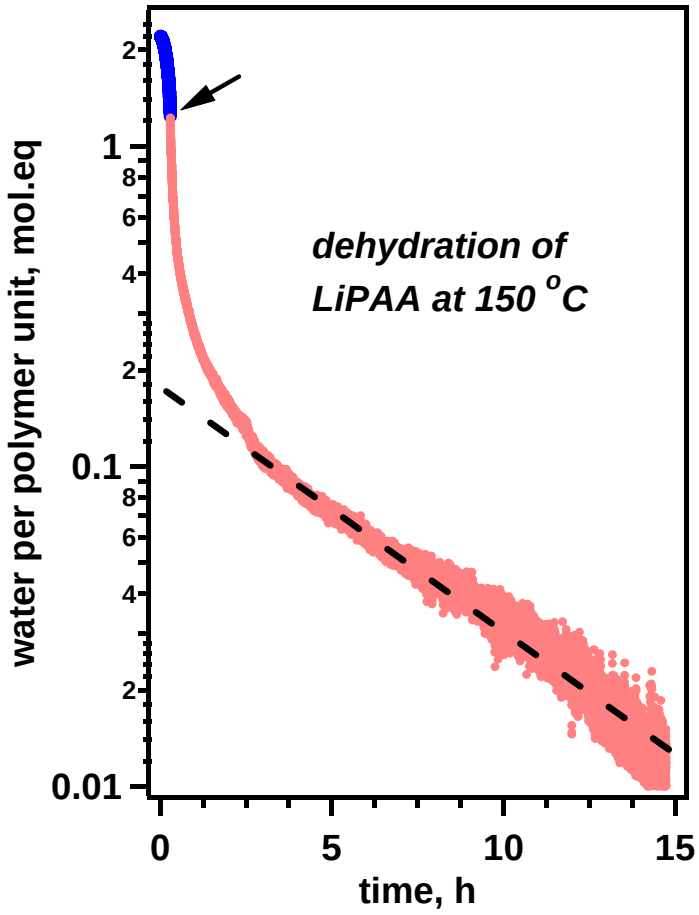

Figure 5. Water loss from hydrated LiPAA binder as observed by thermogravimetry. Note the logarithmic vertical scale. The first section of the plot (indicated with the arrow) corresponds to heating of the sample from 50 to 150 °C at 6 °C/min, whereas the scattered dots indicate the 150 °C isotherm. After the first 3 hours, the mass loss settles into the exponential regime (*dashed line*).

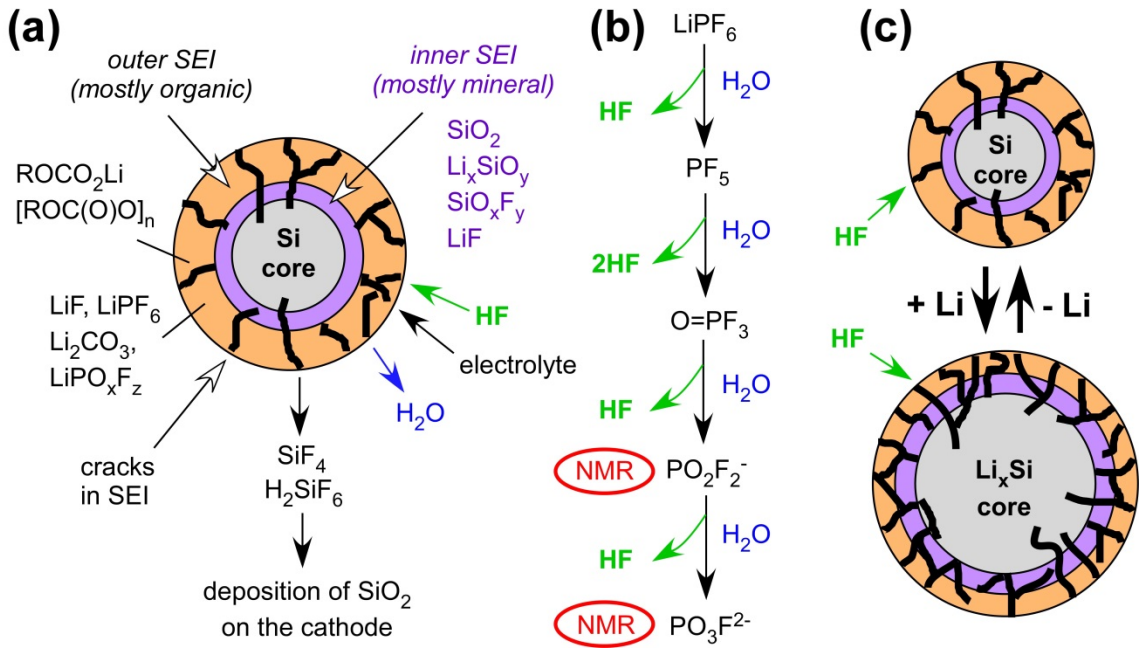

Figure 6. (a) Schematic representation of a Si particle in the advanced stages of aging, with the inner and outer SEI layers formed around the Si core. Mineral compounds derived from Si prevail in the inner SEI while various organic compounds (including alkyl carbonates and inner-carbonate polymers) prevail in the outer SEI, with insoluble salts trapped in the semisolid matrix. Electrolyte and HF molecules can diffuse through the pores and cracks in the outer SEI and react with the particle interior, releasing SiF_4 and water molecules back into the electrolyte. This water joins the hydrolytic cycle for $LiPF_6$ (shown in panel b). In the latter, water sequentially hydrolyzes PO_xF_y species, consuming five water molecules and releasing five HF molecules in total; the released HF can react with Si particles, continuing the hydrolytic cycle. The two species at the end of this sequence can be observed using NMR spectroscopy in the fluids collected from the aged cells. (c) As the Si particles repeatedly expand and contract during lithiation/delithiation, deep cracks develop allowing access of HF to the core, resulting in its digestion and additional SEI formation.

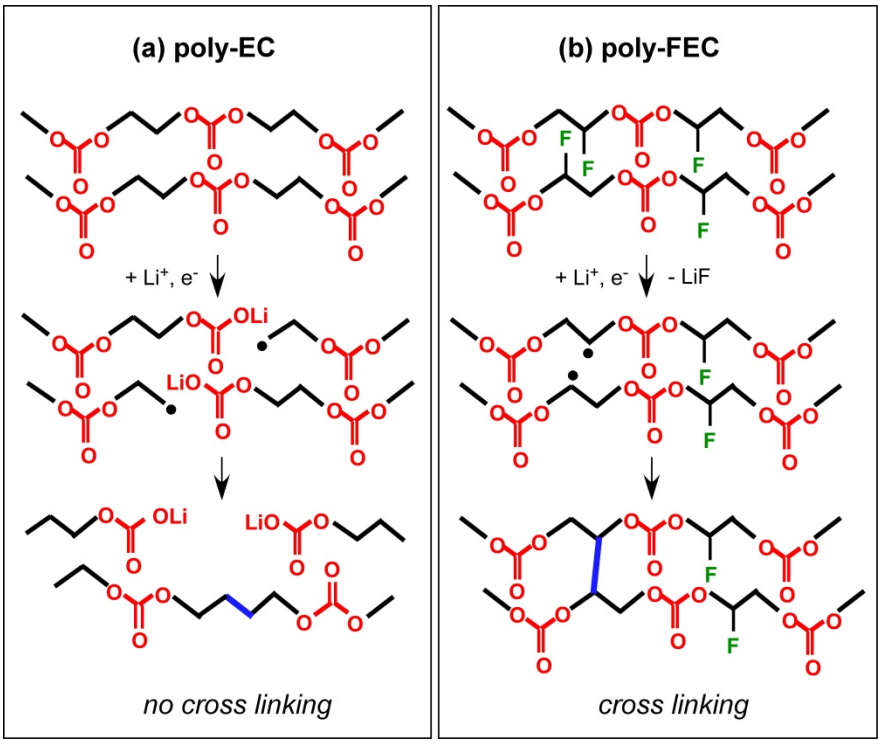

Figure 7. Schematic rationalization of the observed morphological differences between the polymeric component of outer SEI derived from (a) ethylene carbonate (EC) and (b) fluoroethylene carbonate (FEC). In both cases we consider a matrix composed of polycarbonate oligomers generated via anionic polymerization of the corresponding carbonates. Further reduction of the polymer in panel (a) breaks C-O bonds yielding alkylcarbonates and *C*-centered terminal radicals on the neighboring polymer chains. Even if these radicals subsequently recombine, there is no crosslinking, so the cohesion of SEI matrix is not improved. The difference in panel b is that the reduction defluorinates the polymer chains yielding interior radicals whose subsequent recombination links these polymer chains, gradually converting these polymers into an elastomer matrix.

References.

(1) Obrovac, M. N.; Chevrier, V. L. Alloy Negative Electrodes for Li-Ion Batteries. *Chem. Rev.* **2014,** *114*, 11444-11502.

(2) Park, C.-M.; Kim, J.-H.; Kim, H.; Sohn, H.-J. Li-Alloy Based Anode Materials for Li Secondary Batteries. *Chem. Rev.* **2010,** *39*, 3115-3141.

(3) Liang, B.; Liu, Y.; Xu, Y. Silicon-Based Materials as High Capacity Anodes for Next Generation Lithium Ion Batteries. *J. Power Sources* **2014,** *267*, 469-490.

(4) Dupré, N.; Moreau, P.; Vito, E. D.; Quazuguel, L.; Boniface, M.; Bordes, A.; Rudisch, C.; Bayle-Guillemaud, P.; Guyomard, D. Multiprobe Study of the Solid Electrolyte Interphase on Silicon-Based Electrodes in Full-Cell Configuration. *Chem. Mater.* **2016,** *28*, 2557−2572.

(5) Jaumann, T.; Balach, J.; Klose, M.; Oswald, S.; Langklotz, U.; Michaelis, A.; Eckert, J.; Giebeler, L. SEI-Component Formation on Sub 5 nm Sized Silicon Nanoparticles in Li-Ion Batteries: The Role of Electrode Preparation, FEC Addition and Binders. *Phys. Chem. Chem. Phys.* **2015,** *17*, 24956-24967.

(6) Nguyen, D.-T.; Kang, J.; Nam, K.-M.; Paik, Y.; Song, S.-W. Understanding Interfacial Chemistry and Stability for Performance Improvement and Fade of High-Energy Li-Ion Battery of $LiNi_{0.5}Co_{0.2}Mn_{0.3}O_2$//Silicon-Graphite. *J. Power Sources* **2016,** *303*, 150-158.

(7) Philippe, B.; Dedryvère, R.; Gorgoi, M.; Rensmo, H.; Gonbeau, D.; Edstrom, K. Improved Performances of Nanosilicon Electrodes Using the Salt LiFSI: A Photoelectron Spectroscopy Study. *J. Am. Chem. Soc.* **2013,** *135*, 9829−9842.

(8) Philippe, B.; Dedryvère, R.; Gorgoi, M.; Rensmo, H.; Gonbeau, D.; Edstrom, K. Role of the $LiPF_6$ Salt for the Long-Term Stability of Silicon Electrodes in Li-Ion Batteries – a Photoelectron Spectroscopy Study. *Chem. Mater.*. **2013,** *25*, 394-404.

(9) Xu, C.; Lindgren, F.; Philippe, B.; Gorgoi, M.; Björefors, F.; Edstrom, K.; Gustafsson, T. Improved Performance of the Silicon Anode for Li-Ion Batteries: Understanding the Surface Modification Mechanism of Fluoroethylene Carbonate as an Effective Electrolyte Additive. *Chem. Mater.* **2015,** *27*, 2591-2599.

(10) Philippe, B.; Dedryvère, R.; Allouche, J.; Lindgren, F.; Gorgoi, M.; Rensmo, H.; Gonbeau, D.; Edstrom, K. Nanosilicon Electrodes for Lithium-Ion Batteries: Interfacial Mechanisms

Studied by Hard and Soft X-Ray Photoelectron Spectroscopy. *Chem. Mater.* **2012,** *24*, 1107-1115.

(11) Jeschull, F.; Lindgren, F.; Lacey, M. J.; Bjorefors, F.; Edstrom, K.; Brandell, D. Influence of Inactive Electrode Components on Degradation Phenomena in Nano-Si Electrodes for Li-Ion Batteries. *J. Power Sources* **2016,** *325*, 513-524.

(12) An, S. J.; Li, J.; Daniel, C.; Mohanty, D.; Nagpure, S.; Wood III, D. L. The State of Understanding of the Lithium-Ion-Battery Graphite Solid Electrolyte Interphase (SEI) and Its Relationship to Formation Cycling. *Carbon* **2016,** *105*, 52-76.

(13) Schroder, K.; Alvarado, J.; Yersak, T. A.; Li, J.; Dudney, N.; Webb, L. J.; Meng, Y. S.; Stevenson, K. J. The Effect of Fluoroethylene Carbonate as an Additive on the Solid Electrolyte Interphase on Silicon Lithium-Ion Electrodes. *Chem. Mater.* **2015,** *27*, 5531−5542.

(14) Nguyen, C. C.; Yoon, T.; Seo, D. M.; Guduru, P.; Lucht, B. L. Systematic Investigation of Binders for Silicon Anodes: Interactions of Binder with Silicon Particles and Electrolytes and Effects of Binders on Solid Electrolyte Interphase Formation. *ACS Appl. Mater. Interfaces* **2016,** *8*, 12211-12220.

(15) Michan, A. L.; Divitini, G.; Pell, A. J.; Leskes, M.; Ducati, C.; Grey, C. P. Solid Electrolyte Interphase Growth and Capacity Loss in Silicon Electrodes. *J. Am. Chem. Soc.* **2016,** *138*, 7918−7931.

(16) Ferraresi, G.; Czornomaz, L.; Villevieille, C.; Novák, P.; Kazzi, M. E. Elucidating the Surface Reactions of an Amorphous Si Thin Film as a Model Electrode for Li-Ion Batteries. *ACS Appl. Mater. Interfaces* **2016,** *8*, 29791−29798.

(17) Plakhotnyk, A. V.; Ernst, L.; Schmutzler, R. Hydrolysis in the System $LiPF_6$ -Propylene Carbonate- Dimethyl Carbonate - H_2O. *J. Fluor. Chem.* **2005,** *126*, 27-31.

(18) Gueguen, A.; Streich, D.; He, M.; Mendez, M.; Chesneau, F. F.; Novak, P.; Berg, E. J. Decomposition of $LiPF_6$ in High Energy Lithium-Ion Batteries Studied with Online Electrochemical Mass Spectrometry. *J. Electrochem. Soc.* **2016,** *163*, A1095-A1100.

(19) Aurbach, D. Review of Selected Electrode-Solution Interactions Which Determine the Performance of Li and Li Ion Batteries. *J. Power Sources* **2000,** *89*, 206-218.

(20) Campion, C. L.; Li, W. T.; Lucht, B. L. Thermal Decomposition of $LiPF_6$-Based Electrolytes for Lithium-Ion Batteries. *J. Electrochem. Soc.* **2005,** *152*, A2327-A2334.

(21) Li, W. T.; Campion, C.; Lucht, B. L.; Ravdel, B.; DiCarlo, J.; Abraham, K. M. Additives for Stabilizing $LiPF_6$-Based Electrolytes against Thermal Decomposition. *J. Electrochem. Soc.* **2005,** *152*, A1361-A1365.

(22) Burns, J. C.; Sinha, N. N.; Jain, G.; Ye, H.; VanElzen, C. M.; Scott, E.; Xiao, A.; Lamanna, W. M.; Dahn, J. R. The Impact of Intentionally Added Water to the Electrolyte of Li-Ion Cells I. Cells with Graphite Negative Electrodes. *J. Electrochem. Soc.* **2013,** *160*, A2281-A2287.

(23) Yoshida, S.; Masuo, Y.; Shibata, D.; Haruta, M.; Doi, T.; Inabab, M. Adsorbed Water on Nano-Silicon Powder and Its Effects on Charge and Discharge Characteristics as Anode in Lithium-Ion Batteries. *J. Electrochem. Soc.* **2016,** *164*, A6084-A6087.

(24) Magasinski, A.; Zdyrko, B.; Kovalenko, I.; Hertzberg, B.; Burtovyy, R.; Huebner, C. F.; Fuller, T. F.; Luzinov, I.; Yushin, G. Toward Efficient Binders for Li-Ion Battery Si-Based Anodes: Polyacrylic Acid. *ACS Appl. Mater. Interfaces* **2010,** *2*, 3004-3010.

(25) Han, Z.-J.; Yamagiwa, K.; Yabuuchi, N.; Son, J.-Y.; Cui, Y.-T.; Oji, H.; Kogure, A.; Harada, T.; Ishikawa, S.; Aokid, Y., et al. Electrochemical Lithiation Performance and Characterization of Silicon–Graphite Composites with Lithium, Sodium, Potassium, and Ammonium Polyacrylate Binders. *Phys. Chem. Chem. Phys.* **2015,** *17*, 3783-3795.

(26) Bridel, J.-S.; Azaıs, T.; Morcrette, M.; Tarascon, J.-M.; Larcher, D. In Situ Observation and Long-Term Reactivity of Si/C/Cmc Composites Electrodes for Li-Ion Batteries. *J. Electrochem. Soc.* **2011,** *158*, A750-A759.

(27) Markevich, E.; Salitra, G.; Aurbach, D. Fluoroethylene Carbonate as an Important Component for the Formation of an Effective Solid Electrolyte Interphase on Anodes and Cathodes for Advanced Li-Ion Batteries. *ACS Energy Lett.* **2017,** *2*, 1337-1345.

(28) Young, B. T.; Heskett, D. R.; Nguyen, C. C.; Nie, M.; Woicik, J. C.; Lucht, B. L. Hard X-Ray Photoelectron Spectroscopy (HAXPES) Investigation of the Silicon Solid Electrolyte Interphase (SEI) in Lithium-Ion Batteries. *ACS Appl. Mater. Interfaces* **2015,** *7*, 20004-20011.

(29) Michan, A. L.; Parimalam, B. S.; Leskes, M.; Kerber, R. N.; Yoon, T.; Grey, C. P.; Lucht, B. L. Fluoroethylene Carbonate and Vinylene Carbonate Reduction: Understanding Lithium-Ion Battery Electrolyte Additives and Solid Electrolyte Interphase Formation. *Chem. Mater.* **2016,** *28*, 8149−8159.

(30) Trask, S. E.; Pupek, K. Z.; Gilbert, J. A.; Klett, M.; Polzin, B. J.; Jansen, A. N.; Abraham, D. P. Performance of Full Cells Containing Carbonate-Based LiFSI Electrolytes and Silicon-Graphite Negative Electrodes. *J. Electrochem. Soc.* **2016,** *163*, A345-A350.

(31) Klett, M.; Gilbert, J. A.; Pupek, K. Z.; Stephen E. Trask; Abraham, D. P. Layered Oxide, Graphite and Silicon-Graphite Electrodes for Lithium-Ion Cells: Effect of Electrolyte Composition and Cycling Windows. *J. Electrochem. Soc.* **2017,** *164*, A6095-A6102.

(32) Klett, M.; Gilbert, J. A.; Trask, S. E.; Polzin, B. J.; Jansen, A. N.; Dees, D. W.; Abraham, D. P. Electrode Behavior Re-Visited: Monitoring Potential Windows, Capacity Loss, and Impedance Changes in $Li_{1.03}(Ni_{0.5}Co_{0.2}Mn_{0.3})_{0.97}O_2$/Silicon-Graphite Full Cells. *J. Electrochem. Soc.* **2016,** *163*, A875-A887.

(33) Ebel, M. F.; Ebel, H.; Hofmann, A.; Svagera, R. Experimental Determination of Attenuation Lengths of Photo- and Auger Electrons in Silicon Dioxide and in Silicon Nitride in the Energy Range 500 eV < E_{kin} < 3,100 eV. *Surf. Interface Anal.* **1994,** *22*, 51-53.

(34) Louette, P.; Bodino, F.; Pireaux, J.-J. Poly(Acrylic Acid) (PAA). XPS Reference Core Level and Energy Loss Spectra. *Surf. Sci. Spectra* **2005,** *12*, 22-26.

(35) Xu, K.; Zhuang, G. V.; Allen, J. L.; Lee, U.; Zhang, S. S.; Ross, P. N., Jr.; Jow, T. R. Syntheses and Characterization of Lithium Alkyl Mono- and Di-Carbonates as Components of Surface Films in Li-Ion Batteries. *J. Phys. Chem. B* **2006,** *110*, 7708-7719.

(36) Zhuang, G. V.; Xu, K.; Yang, H.; Jow, T. R.; Ross, P. N., Jr. Lithium Ethylene Dicarbonate Identified as the Primary Product of Chemical and Electrochemical Reduction of EC in 1.2 M $LiPF_6$/EC:EMC Electrolyte. *J. Phys. Chem. B* **2005,** *109*, 17567-17573.

(37) Wagner, R.; Korth, M.; Streipert, B.; Kasnatscheew, J.; Gallus, D. R.; Brox, S.; Amereller, M.; Cekic-Laskovic, I.; Winter, M. Impact of Selected $LiPF_6$ Hydrolysis Products on the High Voltage Stability of Lithium-Ion Battery Cells. *ACS Appl. Mater. Interfaces* **2016,** *8*, 30871-30878.

(38) Michan, A. L.; Leskes, M.; Grey, C. P. Voltage Dependent Solid Electrolyte Interphase Formation in Silicon Electrodes: Monitoring the Formation of Organic Decomposition Products. *Chem. Mater.* **2016,** *28*, 385-398.

(39) Gilbert, J. A.; Bareno, J.; Spila, T.; Trask, S. E.; Miller, D. J.; Polzin, B. J.; Jansen, A. N.; Abraham, D. P. Cycling Behavior of NCM523/Graphite Lithium-Ion Cells in the 3–4.4 V

Range: Diagnostic Studies of Full Cells and Harvested Electrodes. *J. Electrochem. Soc.* **2017,** *164*, A6054-A6065.

(40) Hiraoka, K. Hydration and Dehydration of Poly (Acrylic Acid) Lithium Salts. *Reports of the Faculty of Engineering, Nagasaki University* **1981,** *17*, 99-102.

(41) Hiraoka, K.; Yokoyama, T. Hydration of Poly(Acrylic Acid) Lithium Salts. *Polym. Bull.* **1980,** *3*, 225-226.

(42) Hiraoka, K.; Yokoyama, T. Hydration of Poly(Acrylic Acid) Sodium Salts. *Polym. Bull.* **1980,** *2*, 183-188.

(43) Hiraoka, K.; Gotanda, M.; Yokoyama, T. Hydration of Poly(Acrylic Acid) Potassium Salts. *Polym. Bull.* **1980,** *2*, 631-636.

(44) McNeill, I. C.; Sadeghi, S. M. T. Thermal Stability and Degradation Mechanisms of Poly(Acrylic Acid) and Its Salts: Part 2. Sodium and Potassium Salts. *Polym. Degaradion & Stability* **1990,** *30*, 213-230.

(45) Kabanov, V. P.; Dubnitskaya, V. A.; Khar'kov, S. N. Thermal Properties of Polyacrylic Acid. *Polymer Sci. USSR* **1975,** *17*, 1848-1855.

(46) McNeill, I. C.; Sadeghi, S. M. T. Thermal Stability and Degradation Mechanisms of Poly(Acrylic Acid) and Its Salts: Part 1. Poly(Acrylic Acid). *Polym. Degaradion & Stability* **1990,** *29*, 233-246.

(47) An, S. J.; Li, J.; Sheng, Y.; Daniel, C.; Wood III, D. L. Long-Term Lithium-Ion Battery Performance Improvement via Ultraviolet Light Treatment of the Graphite Anode. *J. Electrochem. Soc.* **2016,** *163*, A2866-A2875.

(48) Holleman, A. F.; Wiberg, E., *Holleman-Wiberg: Inorganic Chemistry*. Academic Press: San Diego, 2001.

(49) Pong, T. K.; Besida, J.; O'Donnell, T. A.; Wood, D. G. A Novel Fluoride Process for Producing TiO_2 from Titaniferous Ore. *Ind. Eng. Chem. Res.* **1995,** *34*, 308-313.

(50) Bodenes, L.; Dedryvere, R.; Martinez, H.; Fischer, F.; Tessier, C.; Peres, J.-P. Lithium-Ion Batteriesworking at 85 C: Aging Phenomena and Electrode/Electrolyte Interfaces Studied by XPS. *J. Electrochem. Soc.* **2012,** *159*, A1739-A1746.

(51) Smith, A. J.; Burns, J. C.; Zhao, X.; Xiong, D.; Dahn, J. R. A High Precision Coulometry Study of the SEI Growth in Li/Graphite Cells. *J. Electrochem. Soc.* **2011,** *158*, A447-A452.

(52) Pinson, M. B.; Bazant, M. Z. Theory of SEI Formation in Rechargeable Batteries: Capacity Fade, Accelerated Aging and Lifetime Prediction. *J. Electrochem. Soc.* **2013,** *160*, A243-A250.

(53) Broussely, M.; Herreyre, S.; Biensan, P.; Kasztejna, P.; Nechev, K.; Staniewicz, R. J. Aging Mechanism in Li Ion Cells and Calendar Life Predictions. *J. Power Sources* **2001,** *97-98*, 13-21.

(54) Ploehn, H. J.; Ramadass, P.; White, R. E. Solvent Diffusion Model for Aging of Lithium-Ion Battery Cells. *J. Electrochem. Soc.* **2004,** *151*, A456-A462.

(55) Shkrob, I. A.; Wishart, J. F.; Abraham, D. P. What Makes Fluoroethylene Carbonate Different? *J. Phys. Chem. C* **2015,** *119*, 14954-14964.

(56) Shkrob, I. A.; Zhu, Y.; Abraham, D. P. Reduction of Carbonate Electrolytes and the Formation of Solid-Electrolyte Interface (SEI) in Lithium Batteries. 2. Radiolytically Induced Polymerization of Ethylene Carbonate. *J. Phys. Chem. C* **2013,** *117*, 19270-19279.

(57) Shkrob, I. A.; Zhu, Y.; Abraham, D. P. Reduction of Carbonate Electrolytes and the Formation of Solid-Electrolyte Interface (SEI) in Lithium Ion Batteries. 1. Spectroscopic Observations of Radical Intermediates Generated in One-Electron Reduction of Carbonates. *J. Phys. Chem. C* **2013,** *117*, 19255-19269.

(58) Shkrob, I. A.; Pupek, K. Z.; Abraham, D. P. Allotropic Control: How Certain Fluorinated Carbonate Electrolytes Protect Aluminum Current Collectors by Promoting the Formation of Insoluble Coordination Polymers. *J. Phys. Chem. C* **2016,** *120*, 18435-18444.

(59) Markovsky, B.; Amalraj, F.; Gottlieb, H. E.; Gofer, Y.; Martha, S. K.; Aurbach, D. On the Electrochemical Behavior of Aluminum Electrodes in Nonaqueous Electrolyte Solutions of Lithium Salts. *J. Electrochem. Soc.* **2010,** *157*, A423-A429.

(60) Yang, H.; Kwon, K.; Devine, T. M.; Evans, J. W. Aluminum Corrosion in Lithium Batteries. An Investigation Using the Electrochemical Quartz Crystal Microbalance. *J. Electrochem. Soc.* **2000,** *147*, 4399-4407.

(61) Xu, K. Nonaqueous Liquid Electrolytes for Lithium-Based Rechargeable Batteries. *Chem. Rev.* **2004,** *104*, 4303-4417.

TOC Graphic.

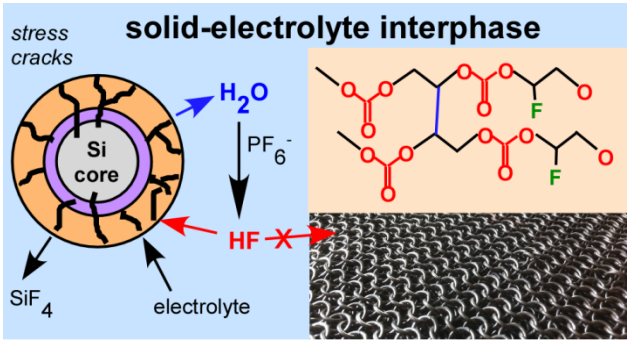
solid-electrolyte interphase
stress cracks
Si core
H_2O
PF_6^-
HF
SiF_4
electrolyte
F
F

Supplementary Information.

Capacity Fade and Its Mitigation in Li-ion Cells with Silicon-Graphite Electrodes

Javier Bareño, Ilya A. Shkrob,* James A. Gilbert, Matilda Klett, and Daniel P. Abraham*

Chemical Sciences and Engineering Division, Argonne National Laboratory, Argonne, Illinois, 60439, USA

Daniel P. Abraham (abraham@anl.gov); Phone: 630-252-4332

Ilya A. Shkrob (shkrob@anl.gov); Phone: 630-252-9516

Table S1.

Details of Composition and Characteristics of Electrodes Used in this Study.

Electrode	Positive	Negative	Negative
Type	**NCM523**	**Si-Gr**	**Gr**
Active material	90 wt% NCM523 (Toda)	73 wt% Graphite (Hitachi MAGE) + 15 wt% Si, 50-70 nm (NanoAmor)	88 wt% Graphite (Hitachi MAGE)
Carbon black (C45, Timcal)	5 wt%	2 wt%	2 wt%
Binder	5 wt% PVdF (Solvay 5130)	10 wt% LiPAA (Argonne)	10 wt% LiPAA (Argonne)
Current collector material	Al	Cu	Cu
Current collector thickness, μm	20	10	10
Loading (coating), mg/cm^2	11.3	2.9	6.4
Loading (active), mg/cm^2	10.2	2.6 [a]	5.76
Electrode porosity, %	33.5	42.4	34.1
Coating, thickness, μm	42	25	48

a) active components include graphite, silicon, and C45 carbon black.

Table S2

Speciation of Fluorinated Phosphate Species in Electrolytes Harvested After Cycling of Cells Containing 0 or 10 wt% FEC in Gen 2 Electrolyte. [a,b] Chemical shifts δ (in parts per million vs. the indicated standard) and spin-spin ($J[^{31}P\text{-}^{19}F]$) coupling constants (in Hz) are also given.

	$\delta(^{19}F)$, ppm *vs.* $CFCl_3$	$\delta(^{31}P)$, ppm *vs.* H_3PO_4	$J[^{31}P\text{-}^{19}F]$, Hz	No FEC		10 wt% FEC	
FEC, wt%				0		10	
				mole % by NMR			
Anion				^{31}P	^{19}F	^{31}P	^{19}F
PF_6^-	-70.17	-114.23	711.4	48.5	48.5	38.9	37.8
$PO_2F_2^-$	-78.56	-15.81	948.3	43.7	45.1	52.9	48.0
PO_3F^{2-}	-71.64	-7.29	911.6	7.8	6.4	7.4	14.1

a) In control experiments, small hydrolytic loss (< 3%) was observed during cell storage, but it was minor relative to the one observed in the fluids harvested after long cycling. The fluids extracted from the Si-Gr batteries at the end of cycle-life testing appeared black and contained suspended particles, including the dislodged silicon and carbon nanoparticles, which do not centrifuge out of the solution; these particles did not interfere with our solution NMR measurements. For the measurements, the aliquots were diluted 1:20 v/v with acetonitrile-d_3.

b) From cells with 20.3 cm^2 electrodes.

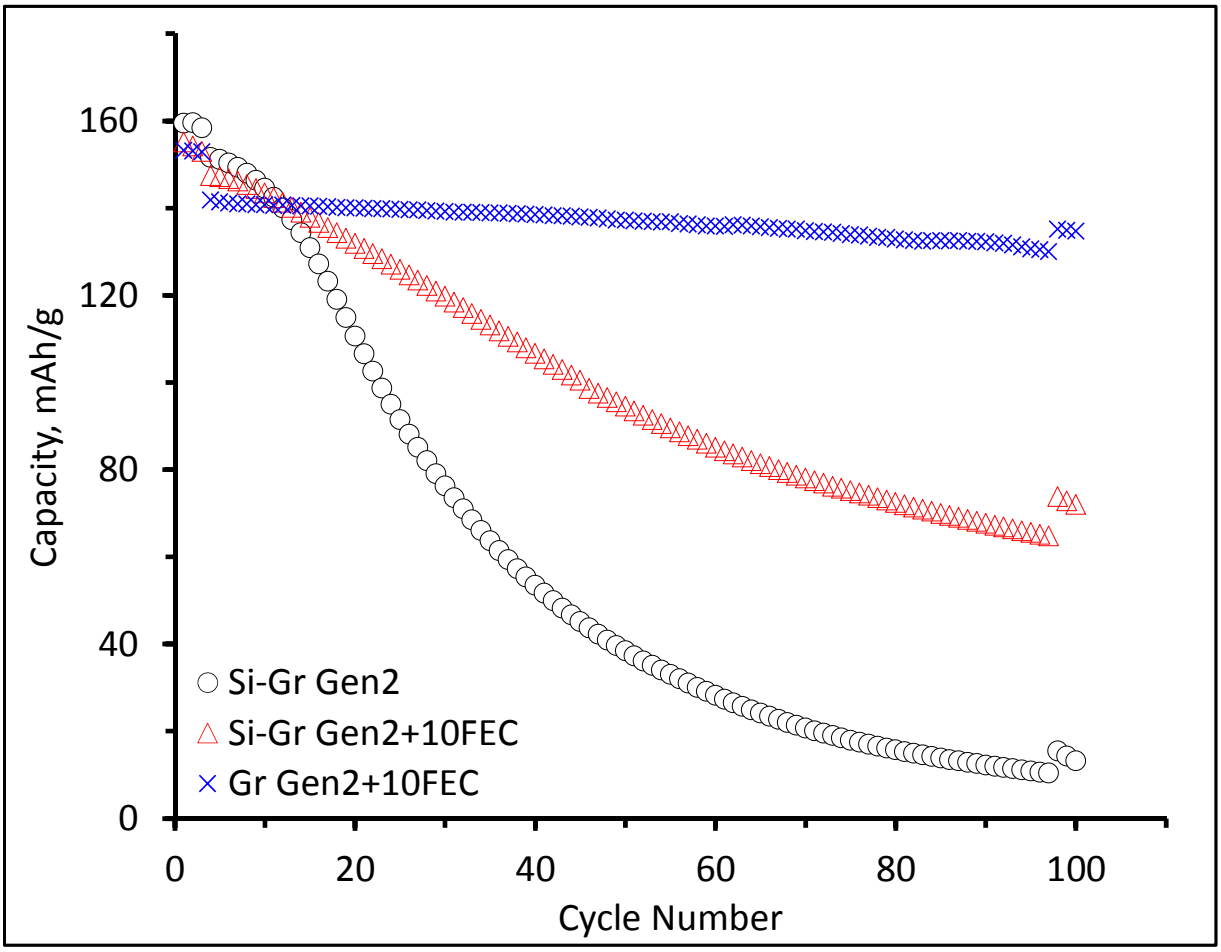

Figure S1. Specific capacity (per weight of NCM523 in positive electrode) vs. cycle number plots for NCM523/Si-Gr full cells with Gen2 electrolyte (black) and with Gen2+10 wt% FEC electrolyte (red). Also shown is data from a NCM523/Gr full cell with Gen2 +10 wt% FEC electrolyte (blue). Note that the cells containing Si show faster capacity decline.

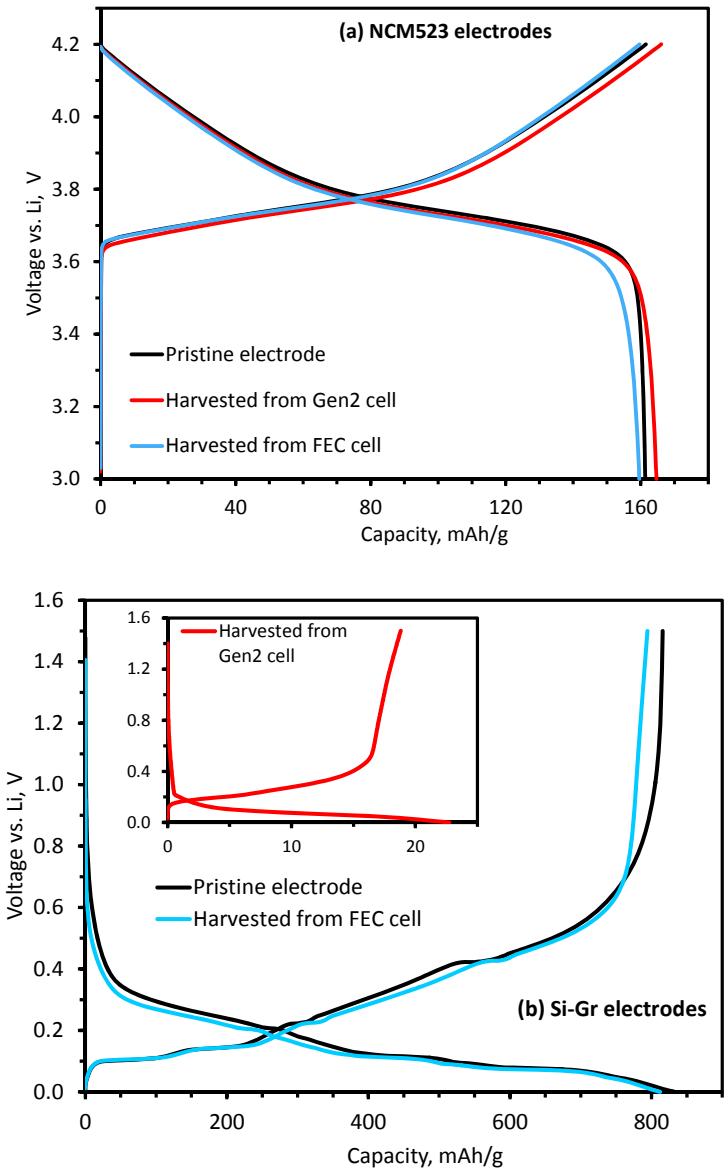

Figure S2. The data for half cells assembled using electrodes harvested from the 100 cycle NCM523/Si-Gr cells and pairing them with Li foil using fresh separators and electrolyte. Cells containing the positive electrode were cycled from 3.0 V to 4.2 V vs. Li/Li^+, and cells containing the negative electrode from 1.5 V to 5 mV vs. Li/Li^+, at < C/20 rates. The harvested electrode data were then compared with data from half cells prepared with pristine positive and negative electrodes cycled under the same conditions. Capacity-voltage profiles for (a) positive and (b) negative electrodes. In (a) it is seen that harvested-electrode-capacities are comparable to that of the pristine electrode. Panel b shows that the negative electrode harvested from the FEC-cell shows capacity similar to that of the pristine electrode. In contrast, the Gen2-cell (see inset) this electrode shows very low capacity.

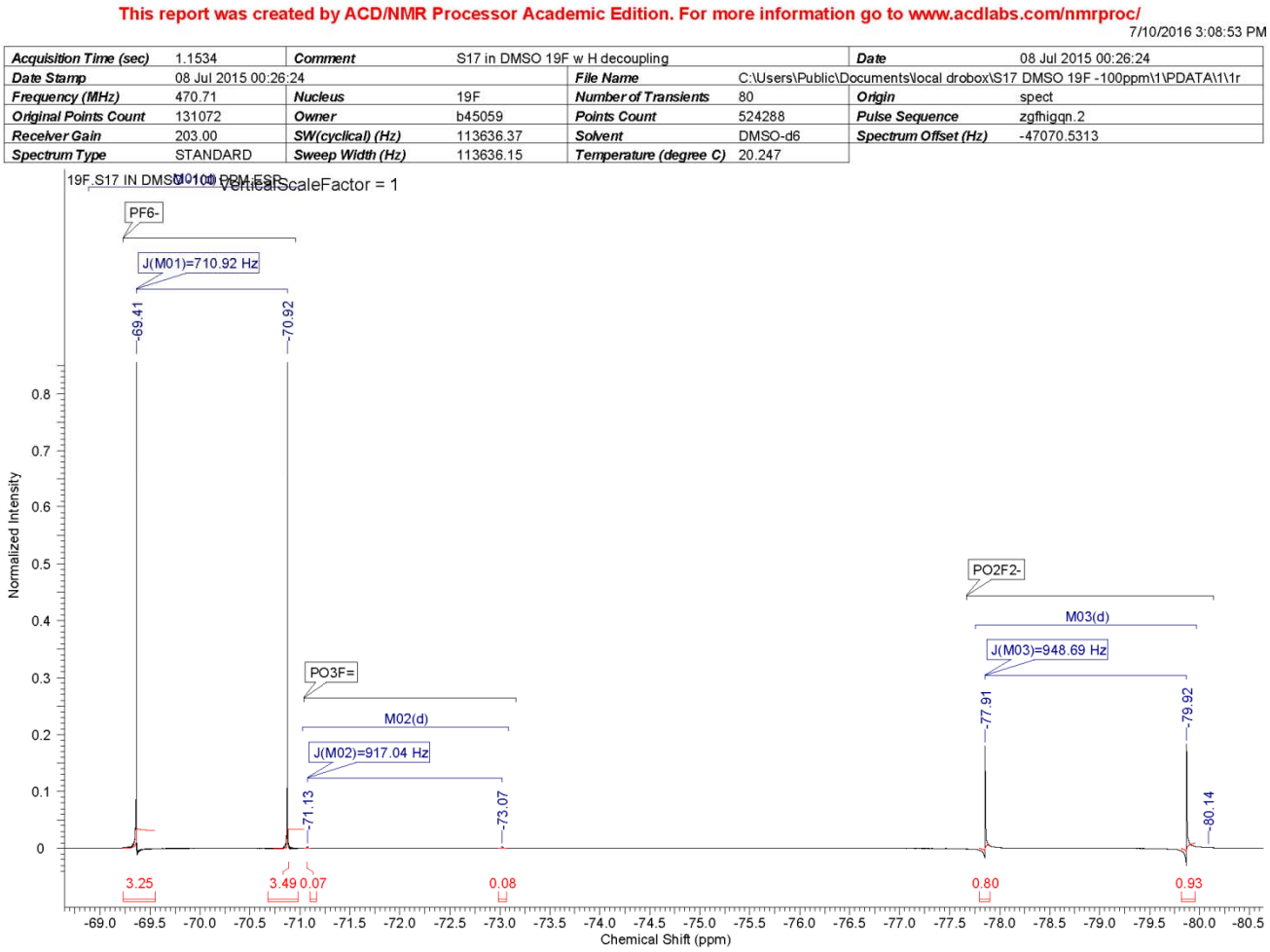

Figure S3. ^{19}F NMR spectrum of electrolyte harvested from a cycled Gen2-cell. Three multiplets of resonance lines from fluorinated phosphate anions are seen in this spectrum (the chemical shifts are given vs. $CFCl_3$).

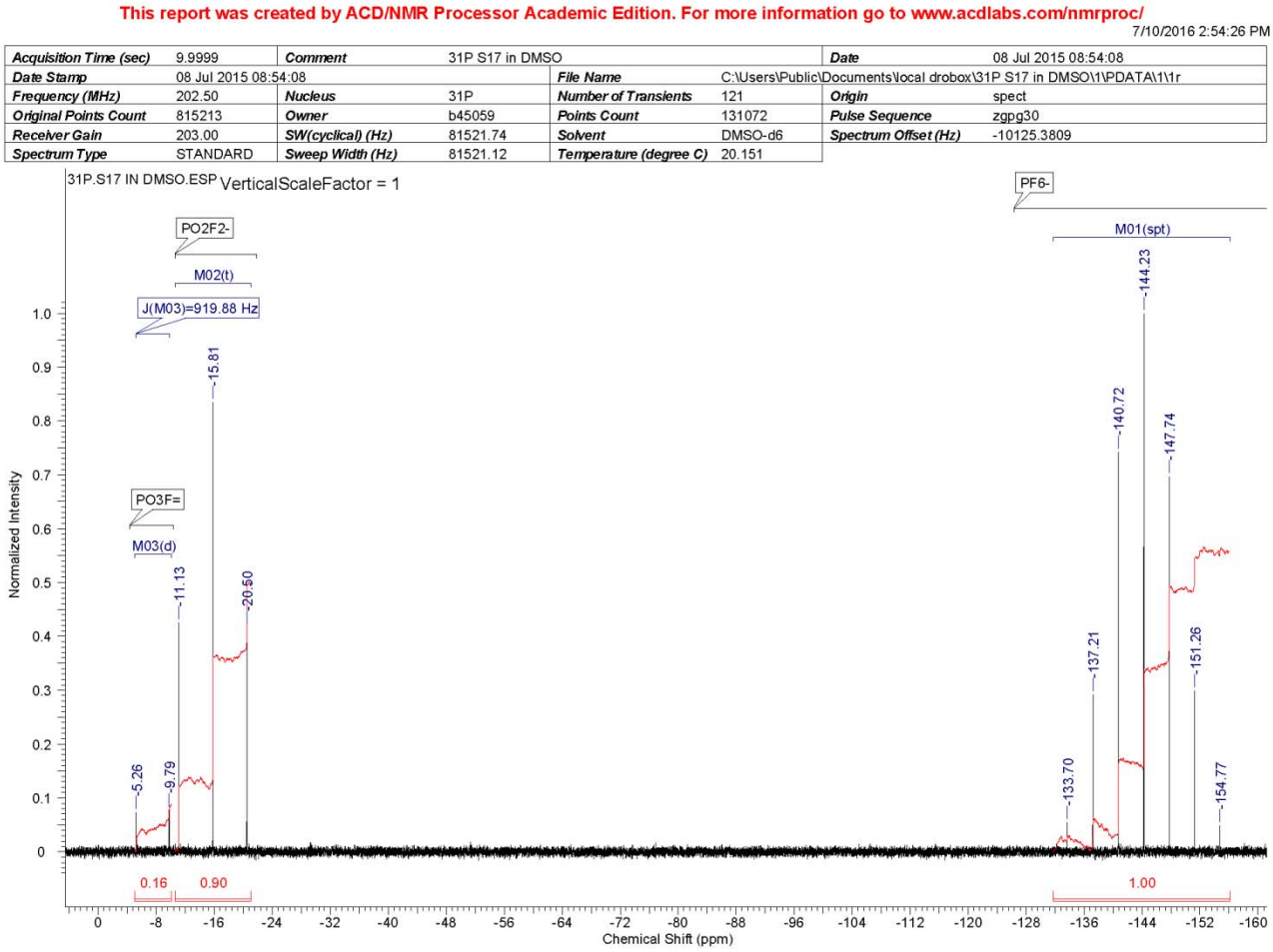

Figure S4. ^{31}P NMR spectrum of electrolyte harvested from a cycled Gen2-cell. Three multiplets of resonance lines from fluorinated phosphate anions are seen in this spectrum (the chemical shifts are given vs. aqueous H_3PO_3).

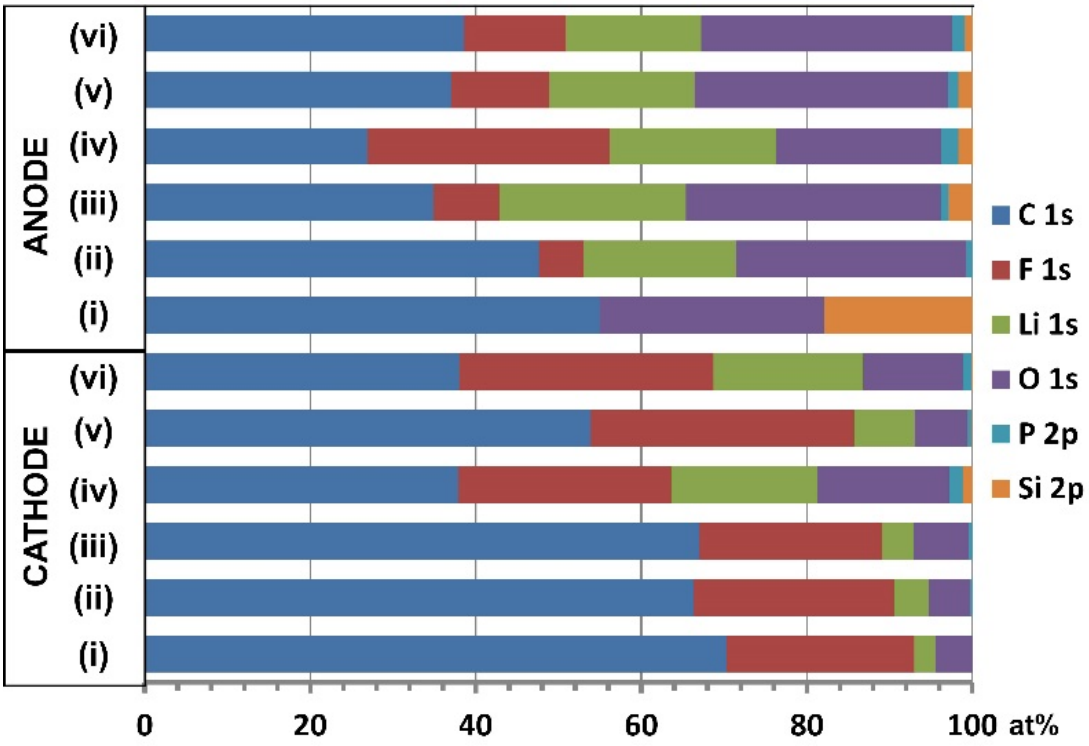

Figure S5. Surface chemical composition (in at%) of electrodes (numbered as in Table 1) harvested from NCM523/Si-Gr (or Gr) cells, obtained from our XPS analyses. The elements (and XPS regions) are indicated in the legend to the right.